Multidimensional traction force microscopy reveals out-of-plane rotational moments about focal adhesions

Wesley R. Legant[a,1], Colin K. Choi[a,1], Jordan S. Miller[a], Lin Shao[b], Liang Gao[b], Eric Betzig[b], and Christopher S. Chen[a,2]

[a]Department of Bioengineering, University of Pennsylvania, Philadelphia, PA 19104; and [b]Janelia Farm Research Campus, Howard Hughes Medical Institute, Ashburn, VA 20147

Recent methods have revealed that cells on planar substrates exert both shear (in-plane) and normal (out-of-plane) tractions against the extracellular matrix (ECM). However, the location and origin of the normal tractions with respect to the adhesive and cytoskeletal elements of cells have not been elucidated. We developed a high-spatiotemporal-resolution, multidimensional (2.5D) traction force microscopy to measure and model the full 3D nature of cellular forces on planar 2D surfaces. We show that shear tractions are centered under elongated focal adhesions whereas upward and downward normal tractions are detected on distal (toward the cell edge) and proximal (toward the cell body) ends of adhesions, respectively. Together, these forces produce significant rotational moments about focal adhesions in both protruding and retracting peripheral regions. Temporal 2.5D traction force microscopy analysis of migrating and spreading cells shows that these rotational moments are highly dynamic, propagating outward with the leading edge of the cell. Finally, we developed a finite element model to examine how rotational moments could be generated about focal adhesions in a thin lamella. Our model suggests that rotational moments can be generated largely via shear lag transfer to the underlying ECM from actomyosin contractility applied at the intracellular surface of a rigid adhesion of finite thickness. Together, these data demonstrate and probe the origin of a previously unappreciated multidimensional stress profile associated with adhesions and highlight the importance of new approaches to characterize cellular forces.

cell mechanics | mechanotransduction | migration | actin

Understanding how cells generate and respond to mechanical forces is critical in cell biology. In anchorage-dependent cells, myosin-II cross-links and contracts actin filaments to generate tension, which is transmitted to the extracellular matrix (ECM) via integrin-mediated adhesions (1–4). The traction stresses (force per area) exerted between adhesions and the ECM drive cell spreading and migration in morphogenesis (5, 6), wound healing (7), and tumor metastasis (8, 9). In addition, these stresses induce changes in adhesion signaling, cytoskeletal reorganization, and gene expression (4, 10–13), thereby regulating functions such as proliferation (14, 15) and differentiation (16, 17).

Measurements of cellular traction stresses have advanced our understanding of mechanotransduction and enabled quantitative modeling of cellular interactions with the ECM (18–20). These measurements reveal that cells exert inwardly oriented tractions at their periphery, where focal adhesions grow centripetally (3, 4, 21). However, the vast majority of methods (collectively termed traction force microscopy, TFM) have assumed that cells exert only shear forces (parallel to the plane of the substrate). Interestingly, recent studies have demonstrated that cells on planar substrata exert significant vertical (normal) tractions, indicating that patterns of cellular force generation are more complex than previously thought (22–25). However, mapping these multidimensional traction stresses with a high spatiotemporal resolution has been challenging, and there is no clear agreement on the dynamics and the location of the normal stresses. Thus, how normal and

shear traction stresses are integrated and what type of net forces are produced relative to focal adhesions and the actin cytoskeleton remain poorly understood.

In this study, we developed a high-resolution 2.5D TFM [measurement of 3D forces exerted by cells on 2D planar surfaces, as opposed to cells fully encapsulated within a 3D matrix (26)] to explore the precise nature of cellular forces applied to the ECM. After fully characterizing the resolution of both the shear and normal tractions using numerical simulations, we applied this approach to mouse embryo fibroblasts (MEFs) expressing EGFP-tagged paxillin, actin, or plasma membrane to measure the multidimensional traction stresses associated with focal adhesions and the actin cytoskeleton. In addition, we generated a finite element model (FEM) of the focal adhesion and pliable substrate and performed 3D super-resolution imaging to explore the most plausible means by which such moments may be generated subject to geometrical constraints within a very thin (200–300 nm) cellular lamella.

Results

To observe the distribution of 3D substrate deformations relative to cytoskeletal structures, we investigated MEFs expressing EGFP-actin cultured on arginine-glycine-aspartic acid-serine (RGDS)–conjugated PEG hydrogels containing fluorescent beads (Fig. 1A and Movie S1). The elastic modulus of hydrogels used in this study was 6,500 Pa, unless specified otherwise. MEFs on PEG hydrogels assumed morphologies comparable to those on traditional culture substrates (e.g., glass or plastic), exhibiting anisotropic protrusions and polarization. Cells were flat; super-resolution structured illumination microscopy (SIM) showed that lamellae are ~180–280 nm tall, whereas the primary increase in height (up to 2–3 μm) occurs only near the nucleus (SI Appendix, Fig. S1). The 3D displacement field within the substrate was determined by tracking beads before and after lysing the cell with detergent. We observed significant in-plane and out-of-plane displacements underneath the thin cell periphery, whereas no displacements (neither in-plane nor out-of-plane) could be detected under the cell nucleus (Fig. 1 B and C and Movie S2). In agreement with previous implementations of 2D traction force microscopy (2D TFM), the shear components of the displacements were also present only at the cell periphery (3, 21). Closer inspection of the vertical displacements revealed that cells pull the hydrogel
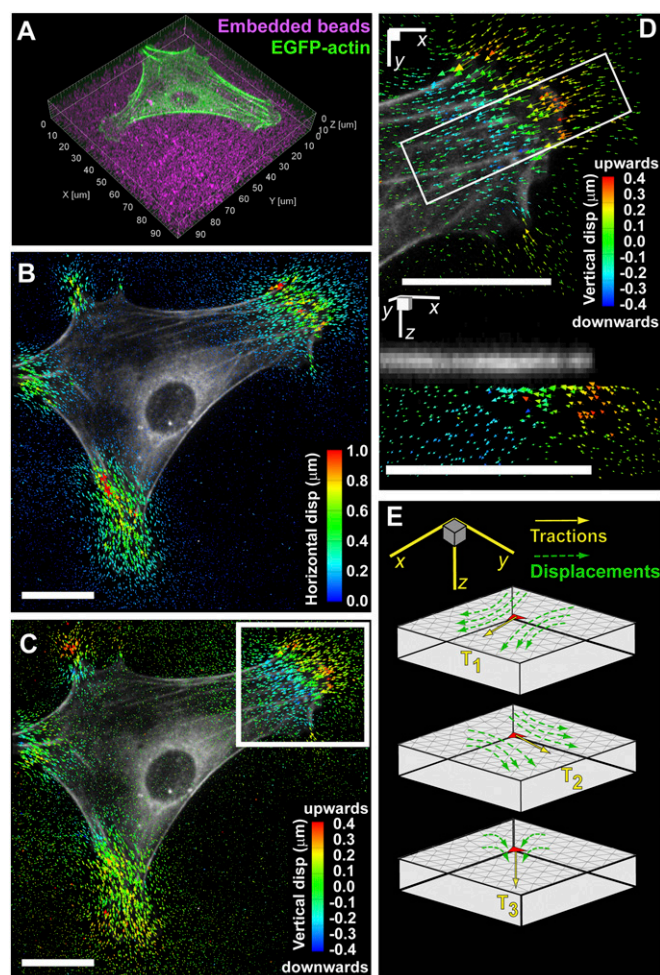
ENGINEERING

CELL BIOLOGY

Fig. 1. Experimental setup and computational methods. (*A*) Volume rendering of an EGFP-actin–expressing mouse embryonic fibroblast (MEF) fully spread and polarized on a planar PEG hydrogel with fluorescent beads imbedded (magenta). (*B* and *C*) Shear and normal components of bead displacement trajectories color-coded by magnitude. (*D*) Inset outlined in *C* magnified showing the normal component of bead displacement trajectories. The bottom figure is the cross-sectional view of the inset outlined above showing the multidimensional bead displacement trajectories. (*E*) Schematic of the finite element model to reconstruct the Green's function. (All scale bars, 20 μm.)

upward under the leading edge and push downward ~10 μm behind the leading edge (Fig. 1*D*).

To quantify the traction stress from the displacement field, we followed a previously described procedure (26). Briefly, a tetrahedral mesh of the hydrogel volume under the cell was generated. Unit tractions were then applied in each of the Cartesian directions at each facet on the surface, and the induced displacement fields were recorded after solving the forward problem for stress equilibrium (Fig. 1*E*). These traction-displacement mappings were then used to generate a discretized Green's function for the hydrogel volume that can be inverted and regularized [through use of the L-curve criterion (27)] to solve for cell tractions. We characterized both the resolution and sensitivity limits of the shear and normal traction reconstructions under experimentally relevant levels of noise, bead density, and material properties (*SI Appendix*, Figs. S2–S12). Our approach was able to capture spatially isolated loadings with a full-width half-maximum of ~10 μm and traction magnitudes down to 300 Pa. Tractions distributed over smaller spatial regions were significantly underestimated and spatially averaged (*SI Appendix*, Figs. S5–S8). We

also investigated our ability to recover sinusoidally oscillating loadings with wavelengths between 5 and 20 μm (*SI Appendix*, Figs. S9–S12) and were able to recover oscillatory loadings of 130 Pa at wavelengths of 14 μm. Although the average element area of the grid on which tractions are computed is significantly smaller (~0.9 μm^2), this information does not fully capture the traction resolution (analogous to how the pixel size of a camera does not necessarily reflect the resolution to optically resolve two point sources in an image). In contrast, the combination of simulated loadings and an experimentally relevant recovery process accurately captures both the spatial resolution and sensitivity of the reported tractions. It should be noted that for sinusoidally oscillating loadings the traction resolution is anisotropic; recovered normal tractions and shear tractions that are directed orthogonal to the spatial axis of variation had ~25% lower errors than shear tractions directed parallel to the axis of spatial variation (*SI Appendix*, Fig. S10). Finally, reported tractions in the range of 100–300 Pa that are near the 10-μm resolution limit likely represent an underestimated and spatially blurred description of the true traction field but are still statistically significant (as confirmed by a bootstrap analysis of the reported tractions) (*SI Appendix*, Fig. S13). *SI Appendix* contains a complete discussion of resolution, sensitivity, and significance.

Applying this approach to cell-induced displacement fields, we found that both shear and normal cellular traction stresses were limited to the cell periphery, whereas negligible tractions were detected in the perinuclear and nuclear regions (Fig. 2*A* and *B* and Movie S3). Maximum shear tractions (550 Pa) occurred at the termini of stress fibers (Fig. 2*C*); however, highest upward and downward normal tractions were concentrated ~5 μm distal (toward the cell periphery) and 5 μm proximal (toward the cell center) to the stress fiber ends, respectively (Fig. 2*D* and Movie S3). These normal tractions (±250 Pa) were typically 30–50% of shear values. Variation of the regularization parameter used for traction reconstruction changed the overall magnitude of both shear and normal forces but did not alter the general conclusions (*SI Appendix*, Fig. S14). These findings suggested that torque was being applied to the substrate in the vicinity of focal adhesions, which anchor the ends of stress fibers and serve as the primary force-transmitting structure to the ECM. To investigate this possibility, we transfected MEFs with paxillin-EGFP, an adapter protein that localizes to integrin-mediated adhesions (28). We observed paxillin-EGFP–containing focal adhesions near the cell periphery and maximal shear tractions directly under the adhesions (Fig. 2*E* and *G*). Moreover, we detected upward and downward traction stresses just distal and proximal of the adhesions, respectively, indicating that focal adhesions indeed served as pivot points for rotational moments (Fig. 2*F* and *H*). These moments were present at focal adhesions in both the leading lamella and in retracting extensions of cells (Fig. 2*E* and *F*), and their magnitudes mirrored changes in adhesion density (number of adhesions per unit area) due to growth and disassembly (Movies S4 and S5). Taken together, these results reveal that shear tractions and rotational moments are generated under and around focal adhesions, respectively, demonstrating a more complex and intrinsic force distribution than described previously (3, 19, 29).

To examine how rotational moments around focal adhesions evolved during dynamic cellular processes, we acquired time-lapse volumetric stacks during migration and initial spreading. MEFs were transfected with mEGFP-farnesyl to visualize cell morphology dynamics (Movie S6). Similar to stationary cells, both migrating and spreading cells generated rotational moments localized to both protruding and retracting regions with normal tractions reaching ~±350 Pa. In migrating cells, we found that both shear and normal tractions moved with the extending leading edge (Fig. 3 *A* and *B* and Movies S7 and S8). This dynamic colocalization of force distributions at the cell periphery was also observed during cell spreading. Cells spread initially in an isotropic manner and flatten against the substrate as they become polarized, similar to what has
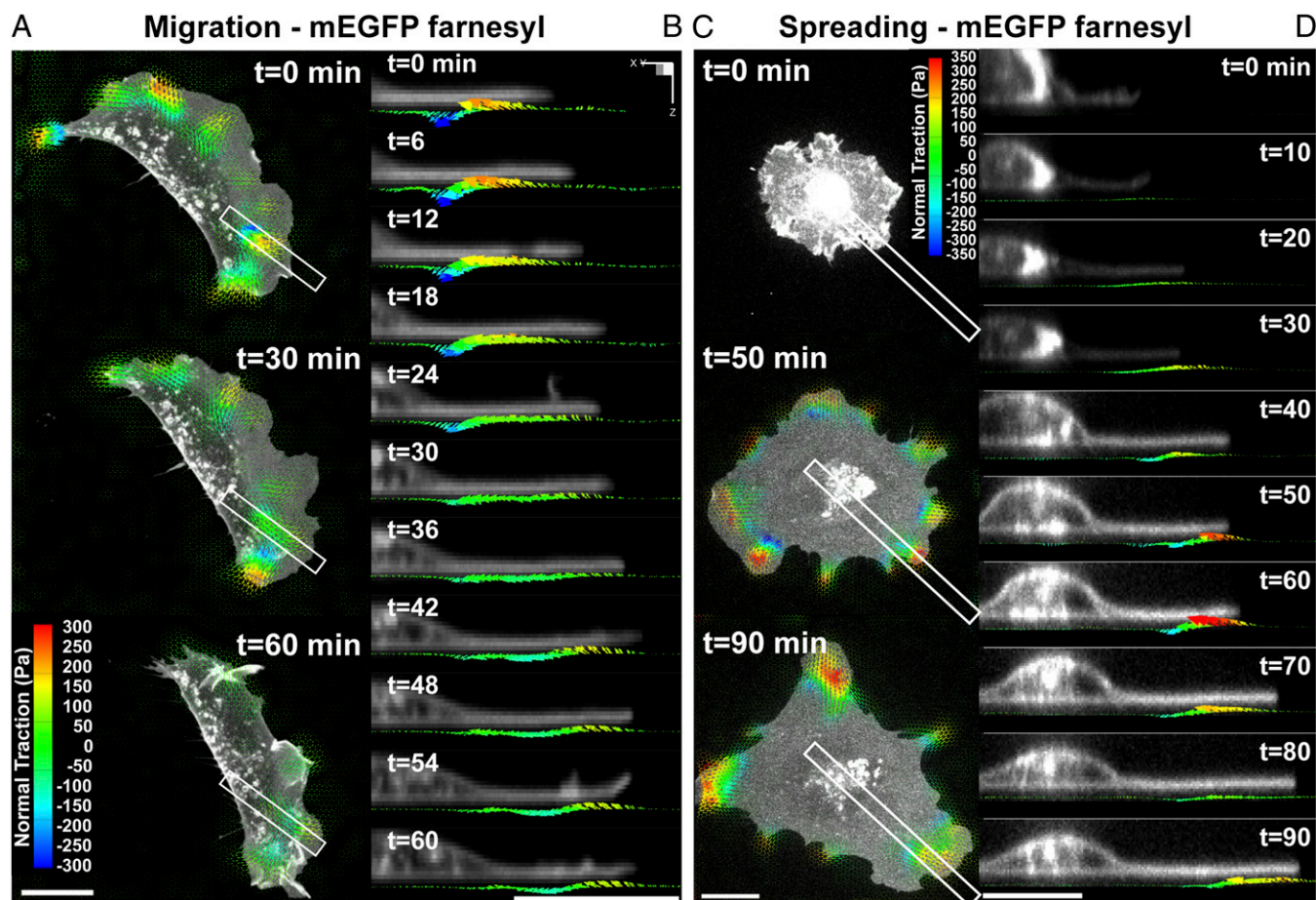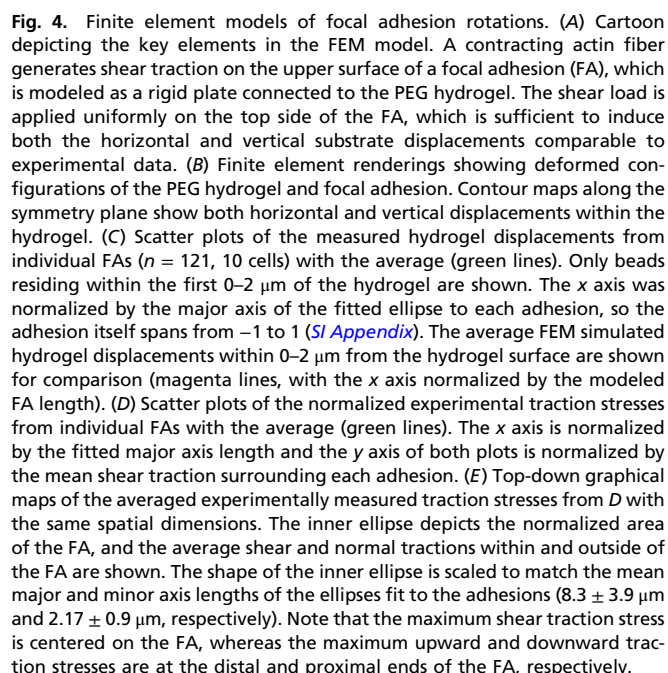
been previously described (30). We observed the simultaneous emergence of both shear and normal tractions shortly (~20 min) after cells adhered to the substrate (Fig. 3 C and D). Both the shear and normal tractions were restricted to the leading lamella and increased substantially during the first hour of spreading. In contrast to previous studies that showed substantial downward compression under the nucleus, we found no tractions under the cell nucleus, but observed instead the presence of outward "waves" of rotational tractions that perhaps emerged initially in the perinuclear region but quickly propagated outward, remaining localized with the leading edge (Fig. 3D and Movies S9 and S10).

Because it was not immediately apparent how focal adhesions in a thin (~200 nm tall) cellular lamella could generate substantial out-of-plane moments, we generated a FEM derived from our current knowledge of cell adhesions. Based on a recent interferometric photoactivated localization microscopy (iPALM) study (31) and our SIM data (SI Appendix, Fig. S1), the focal adhesion was set at 150 nm in height and physically coupled to the elastic PEG hydrogel, which was modeled as a Neo-Hookean solid (SI Appendix, Fig. S15). In the simplest scenario, we applied a uniform shear load to the top surface of the adhesion plate to mimic actin-myosin filaments pulling on adhesions (1, 4, 12, 20) (Fig. 4A). The magnitude of this load was then scaled to induce a lateral ECM displacement of similar magnitude (~0.5 μm) to what was observed experimentally. We found that rotational moments could be generated only if the adhesion were significantly stiffer than the underlying substrate (SI Appendix). In this setting, as the material adjacent to the adhesion is compressed, shear lag from the top of the adhesion to the substrate causes the plate to rotate, thereby generating a moment (Fig. 4B). With this model, a lateral ECM displacement of 0.5 μm corresponded to ~200 nm vertical displacements generated at the distal and proximal ends of the adhesion (Fig. 4 B and C). These vertical displacements matched well with the experimentally observed results (averaged over 120 focal adhesions in 10 different cells), consistent with a model in which the focal adhesion rotation is generated primarily by horizontal tension transmitted by actin stress fibers at the intracellular surface of adhesions. Interestingly, the experimental vertical displacements recovered slowly at the proximal end, which may indicate that other cytoskeletal structures, such as cortical actin, are also contributing to the compression into the ECM, a phenomenon that was not modeled. The nature of shear and normal traction stresses relative to the focal adhesion was highly consistent. Compiling the data from the multiple adhesions, we found that the maximum shear traction is applied symmetrically about the adhesion center (Fig. 4 D and E). In addition, the maximum upward and downward tractions localized to the distal and proximal ends of adhesions, respectively, demonstrating the characteristic rotational moment. Both the shear and normal tractions spread slightly beyond the adhesion boundaries, although it is currently unclear whether this spread is mediated by additional adhesions in the lamellipodium distal to focal adhesions, and/or whether it is due to the smoothing nature of the Green's function that relates substrate displacements to surface tractions (Discussion and SI Appendix).

Discussion

In this study, we developed high-resolution 2.5D TFM to investigate the multidimensional nature of cellular tractions. The spatial resolution and traction sensitivity are inherently interdependent in TFM, and we performed an extensive analysis of this key relationship, including a sensitivity curve that characterizes our method under multiple different loading conditions (SI Appendix, Fig. S8). We anticipate that providing such a curve for each TFM method will allow for comparisons of resolution and sensitivity across methods. We use our 2.5D TFM to demonstrate that cells exert dynamic rotational moments at focal adhesions and associated actin stress fibers. Cells exerted upward forces that were distal and downward

Fig. 2. Multidimensional traction stress and cytoskeletal localization. (A and B) Shear and vertical traction stress vectors generated by a MEF expressing EGFP-actin. The vectors are color-coded by magnitude. Both components of traction stresses are localized to the cell periphery. (C and D) Inset outlined in A magnified showing traction stress vectors color-coded by shear and normal components. Maximum shear tractions are detected at the termini of actin stress fibers, whereas the upward and downward normal tractions are applied in front of and behind the fiber ends, respectively. (E and F) Shear and normal traction stress vectors generated by a MEF expressing paxillin-EGFP are localized to focal adhesions in broad peripheral regions and a narrow retracting tail. (G and H) Inset outlined in E magnified showing shear and normal traction stress vectors relative to focal adhesions. Maximum shear stresses are detected directly over elongated focal adhesions, whereas the upward-to-downward gradient of normal stresses forms a rotational moment around the adhesions. (All scale bars, 20 μm.)

forces proximal to focal adhesions, which thereby served as pivots to mediate a torque on the ECM. The locations, magnitude, and dynamics of these tractions were consistent in polarized cells,

ENGINEERING

CELL BIOLOGY

Fig. 3. Dynamic measurements of 2.5D traction stress. (*A*) Time-lapse images depicting traction stress vectors color-coded by the normal component generated by a migrating MEF expressing mEGFP-farnesyl. As the cell moves (toward right), rotational moments are applied in the protruding front as well as the sides. (*B*) Time-lapse cross-sectional views of the inset outlined in *A* showing dynamic rotational moments that move with the thin protruding cellular body during cell migration. (*C*) Time-lapse images of mEGFP-farnesyl–expressing MEF undergoing spreading. No significant vertical traction stresses are detected until the cell extends thin protrusions and flattens against the substratum. Minimal tractions are detected under the nucleus. (*D*) Time-lapse cross-sectional views of the inset outlined in *C*. Comparable to migrating cells, rotating moments progress outward with the leading edge and remain localized to the cell periphery. (All scale bars, 20 μm.)

migrating cells, and spreading cells. Moreover, the normal tractions occurred at focal adhesions both in protrusions and retracting tails, suggesting that the rotational moment about adhesions is intrinsic to the structural organization of the cell–matrix interface.

Previous studies have reported downward pushing forces into the substrate that suggested a role for nuclear compression (22, 25), but we find minimal forces exerted in the nuclear and perinuclear regions. This discrepancy may result from differences in cell type (fibroblasts vs. endothelial cells or *Dictyostelium*), cell shape (spread vs. round), hydrogel rigidity (~6.5 kPa in this study vs. 400 Pa, ~4 kPa for previous studies), or spatial resolution of the different TFM methods. Indeed, we observed that downward tractions are localized in the nuclear region in cells that are in the early phase of spreading (i.e., cells that are relatively round). A similar pattern of substrate deformation has been reported from a round fluid droplet adhered to a flexible substrate (32, 33), suggesting that surface tension could contribute to this type of deformation. However, as cells spread and flatten out against the substrate, their shape departs dramatically from that of a fluid droplet and normal tractions propagate outward to localize to the cell periphery. When substrate rigidity was decreased, we found that both shear and normal tractions also decreased. Interestingly, the relative magnitude of the normal tractions compared with the shear tractions increased on less rigid hydrogels, indicating that substrate rigidity may modify how the two traction components are transmitted. On

all substrate rigidities, however, shear and normal tractions were exerted primarily near the cell periphery (*SI Appendix*, Fig. S16). We also found in multiple cell types that the shear and normal tractions are exerted at focal adhesions, demonstrating the coupling of focal adhesions and multidimensional traction stresses (*SI Appendix*, Figs. S17 and S18).

The measurements of rotational moments around focal adhesions suggest a more complex pattern of stresses at the cell–ECM interface than is currently appreciated. Cell-generated tension at adhesions has been described largely as in-plane, whereby adhesion growth, actin flow, and traction stresses are coupled and exhibit correlated directional dynamics (2, 3, 21, 34). As a result, mechanotransduction processes at adhesions are proposed to be regulated predominantly by shear forces that stretch adhesion proteins and induce protein–protein interactions and signaling events (13, 19, 20, 29). Our analysis of subadhesion, multidimensional traction stress introduces additional factors to consider. These distinct mechanical loads within a single focal adhesion could contribute to the spatial structure of adhesions, for example by differentially regulating protein binding, conformational changes, and force-induced signaling (35). Tension in the distal end could promote protein unfolding and interactions (e.g., between vinculin, talin, and actin) to mediate a molecular clutch (36–39) or phosphorylation (40), whereas shearing and compression in the proximal end may induce the rapid protein exchanges that mediate focal

Fig. 4. Finite element models of focal adhesion rotations. (*A*) Cartoon depicting the key elements in the FEM model. A contracting actin fiber generates shear traction on the upper surface of a focal adhesion (FA), which is modeled as a rigid plate connected to the PEG hydrogel. The shear load is applied uniformly on the top side of the FA, which is sufficient to induce both the horizontal and vertical substrate displacements comparable to experimental data. (*B*) Finite element renderings showing deformed configurations of the PEG hydrogel and focal adhesion. Contour maps along the symmetry plane show both horizontal and vertical displacements within the hydrogel. (*C*) Scatter plots of the measured hydrogel displacements from individual FAs (n = 121, 10 cells) with the average (green lines). Only beads residing within the first 0–2 μm of the hydrogel are shown. The *x* axis was normalized by the major axis of the fitted ellipse to each adhesion, so the adhesion itself spans from −1 to 1 (*SI Appendix*). The average FEM simulated hydrogel displacements within 0–2 μm from the hydrogel surface are shown for comparison (magenta lines, with the *x* axis normalized by the modeled FA length). (*D*) Scatter plots of the normalized experimental traction stresses from individual FAs with the average (green lines). The *x* axis is normalized by the fitted major axis length and the *y* axis of both plots is normalized by the mean shear traction surrounding each adhesion. (*E*) Top-down graphical maps of the averaged experimentally measured traction stresses from *D* with the same spatial dimensions. The inner ellipse depicts the normalized area of the FA, and the average shear and normal tractions within and outside of the FA are shown. The shape of the inner ellipse is scaled to match the mean major and minor axis lengths of the ellipses fit to the adhesions (8.3 ± 3.9 μm and 2.17 ± 0.9 μm, respectively). Note that the maximum shear traction stress is centered on the FA, whereas the maximum upward and downward traction stresses are at the distal and proximal ends of the FA, respectively.

adhesion elongation (41–44). Adhesion dynamics (turnover and lifetime) and strengthening may also be regulated differently by vertical extension, shear, and compression, depending on the size and the molecular composition of adhesions (4, 20, 45, 46). Thus, in addition to the magnitude and the rate of applied force, knowing how molecules respond to different types of stress will lead to a more complete understanding of adhesion-mediated mechanotransduction.

It is interesting to note that rotational moments have not been observed in cells encapsulated within a 3D hydrogel (26), suggesting that the moments about focal adhesions are characteristic phenomena induced by a 2D ECM. Actin is a key cytoskeletal element that transmits tension to the cell–ECM interface to generate traction stress, and its architecture is dramatically different in 2D and 3D ECMs (47). More recently, 3D super-resolution, stochastic optical reconstruction microscopy showed directly that the dorsal and ventral actin layers have dramatically different architectures in the vicinity of focal adhesions (48). This study also shows the ventral cortex can be buckled, whereas the dorsal layer is relatively smooth. These findings support a model of ventral buckling under compressive loading due to a dorsal contractile element and would agree with the slower ECM displacement recovery observed in our data (compared with our FEM model) measured near the proximal end of focal adhesions. In addition, subresolution nascent adhesions assemble in the lamellipodium and mediate attachment to the substratum at the leading edge (42). These structures may also serve as traction point sources near the distal edge of focal adhesions as actin ruffles and polymerizes, but resolving precise tractions resulting from these structures is beyond our current resolution limits. This 2D-specific organization could contribute to mechanotransduction, migration, and signaling responses uniquely observed in 2D settings (49, 50). In summary, the mappings of multidimensional cellular forces and cytoskeletal structures presented here offer another dimension to current models of cell migration and adhesion mechanobiology (10, 51–54). Future improvements to the spatial and temporal resolution of cell traction measurements in 2.5D and fully 3D settings (26), combined with subdiffraction limit imaging of the 3D cytoskeletal and adhesion architecture (31, 48), will be a critical path toward understanding how cells generate, sense, and respond to mechanical forces in a variety of physiological settings.

Materials and Methods

Cell Culture and Plasmids. Spontaneously immortalized MEFs were cultured in DMEM (Mediatech, Inc.) with 5% (vol/vol) FBS (55) (Richard Assoian, University of Pennsylvania, Philadelphia, PA). MEFs were transfected transiently with paxillin-EGFP [Clare Waterman, National Institutes of Health (NIH), Bethesda, MD], EGFP-actin, and mEGFP-farnesyl-5 [a plasma membrane localized GFP-tagged 20-amino-acid farnesylation signal from c-Ha-Ras (56)] (Michael Davidson, Florida State University, Tallahassee, FL) using Lipofectamine 2000 (Invitrogen) or TransIT-LT1 (Mirus). Cells were plated on hydrogels for at least 3 h to allow spreading before imaging.

Preparation of Deformable Substrates and Mechanical Characterization. PEG-based hydrogels with RGDS were synthesized as described previously (57) and flexible 2D substrates for TFM experiments were polymerized between glass coverslips with UV light. After removal of the top coverslip, the substrates were incubated in PBS at 37 °C for at least 24 h to allow swelling (*SI Appendix*). The Poisson ratio of 0.34 and shear modulus of 2,431 ± 87 Pa for the PEG-based hydrogels was measured as described in (*SI Appendix*, *Fig S3*). The Young's modulus of 6,517 Pa was calculated from the shear modulus using the Poisson ratio of 0.34 and assuming linearly elastic, isotropic material properties.

Image Acquisition. Cells were imaged with a 60×, 1.2 numerical aperture (NA), water immersion objective (UPLSAPO 60XW; Olympus) attached to an Olympus IX71 inverted microscope equipped with a CSU10 spinning disk confocal scan head (Yokogawa Electric Corp.), live cell incubator (Pathology Devices), and an ImagEM 16-bit EMCCD camera (Hamamatsu Photonics) or a LD C-Apochromat 63×, 1.15 NA, water immersion objective attached to a Zeiss Axiovert 200M inverted microscope equipped with a CSU10 spinning disk confocal scan head,

live cell incubator, and a Photometrics Evolve EMCCD camera. A 98- × 98- × 15-μm volume was imaged around each cell to incorporate the entire cell volume and ~10 μm of hydrogel below the cell. These parameters corresponded to voxel dimensions of 0.1917 × 0.1917 × 0.5 μm or 0.1808 × 0.1808 × 0.5 μm in the horizontal and axial planes on the Olympus and Zeiss systems, respectively. After the stressed image was acquired, the cells were treated with 0.5% (wt/vol) SDS detergent (JT Baker), reequilibrated for 10 min, and then reimaged to acquire a reference image of the nonstressed hydrogel. Time-lapse datasets were acquired at time intervals ranging from 30 s to 5 min. Super-resolution structured illumination images were acquired as described previously (58) (*SI Appendix*, Fig S1).

Calculation of Bead Displacements and Cell Tractions. Images were imported into Matlab (MathWorks) and bead centroids were identified using a 3D Gaussian maximum likelihood estimator. After centroid identification, beads in the stressed (subject to cell-generated tractions) dataset were matched to beads in the relaxed (after cell lysis) dataset using a previously described feature vector-based algorithm relating the relative position of each bead to its local neighbors (26). Cell tractions were calculated from the measured bead displacements via a discretized Green's function as described previously (26) and in detail in *SI Appendix*.

Finite Element Modeling. FEM simulations of adhesions were carried out in Abaqus using the finite strain option (NLGEOM) to account for any geometric nonlinearities. The assumptions, parameters and material properties for each condition are detailed in *SI Appendix*.

1. Vicente-Manzanares M, Ma X, Adelstein RS, Horwitz AR (2009) Non-muscle myosin II takes centre stage in cell adhesion and migration. *Nat Rev Mol Cell Biol* 10(11):778–790.
2. Balaban NQ, et al. (2001) Force and focal adhesion assembly: A close relationship studied using elastic micropatterned substrates. *Nat Cell Biol* 3(5):466–472.
3. Beningo KA, Dembo M, Kaverina I, Small JV, Wang YL (2001) Nascent focal adhesions are responsible for the generation of strong propulsive forces in migrating fibroblasts. *J Cell Biol* 153(4):881–888.
4. Parsons JT, Horwitz AR, Schwartz MA (2010) Cell adhesion: Integrating cytoskeletal dynamics and cellular tension. *Nat Rev Mol Cell Biol* 11(9):633–643.
5. Discher DE, Janmey P, Wang YL (2005) Tissue cells feel and respond to the stiffness of their substrate. *Science* 310(5751):1139–1143.
6. Gumbiner BM (1996) Cell adhesion: The molecular basis of tissue architecture and morphogenesis. *Cell* 84(3):345–357.
7. Hinz B, Mastrangelo D, Iselin CE, Chaponnier C, Gabbiani G (2001) Mechanical tension controls granulation tissue contractile activity and myofibroblast differentiation. *Am J Pathol* 159(3):1009–1020.
8. Friedl P, Gilmour D (2009) Collective cell migration in morphogenesis, regeneration and cancer. *Nat Rev Mol Cell Biol* 10(7):445–457.
9. Munevar S, Wang Y, Dembo M (2001) Traction force microscopy of migrating normal and H-ras transformed 3T3 fibroblasts. *Biophys J* 80(4):1744–1757.
10. Schwartz MA (2010) Integrins and extracellular matrix in mechanotransduction. *Cold Spring Harb Perspect Biol* 2(12):a005066.
11. Ingber D (1991) Integrins as mechanochemical transducers. *Curr Opin Cell Biol* 3(5):841–848.
12. Geiger B, Spatz JP, Bershadsky AD (2009) Environmental sensing through focal adhesions. *Nat Rev Mol Cell Biol* 10(1):21–33.
13. Vogel V, Sheetz M (2006) Local force and geometry sensing regulate cell functions. *Nat Rev Mol Cell Biol* 7(4):265–275.
14. Chen CS, Mrksich M, Huang S, Whitesides GM, Ingber DE (1997) Geometric control of cell life and death. *Science* 276(5317):1425–1428.
15. Nelson CM, et al. (2005) Emergent patterns of growth controlled by multicellular form and mechanics. *Proc Natl Acad Sci USA* 102(33):11594–11599.
16. Engler AJ, Sen S, Sweeney HL, Discher DE (2006) Matrix elasticity directs stem cell lineage specification. *Cell* 126(4):677–689.
17. Fu J, et al. (2010) Mechanical regulation of cell function with geometrically modulated elastomeric substrates. *Nat Methods* 7(9):733–736.
18. Sabass B, Gardel ML, Waterman CM, Schwarz US (2008) High resolution traction force microscopy based on experimental and computational advances. *Biophys J* 94(1):207–220.
19. Hoffman BD, Grashoff C, Schwartz MA (2011) Dynamic molecular processes mediate cellular mechanotransduction. *Nature* 475(7356):316–323.
20. Gardel ML, Schneider IC, Aratyn-Schaus Y, Waterman CM (2010) Mechanical integration of actin and adhesion dynamics in cell migration. *Annu Rev Cell Dev Biol* 26:315–333.
21. Aratyn-Schaus Y, Gardel ML (2010) Transient frictional slip between integrin and the ECM in focal adhesions under myosin II tension. *Curr Biol* 20(13):1145–1153.
22. Delanoë-Ayari H, Rieu JP, Sano M (2010) 4D traction force microscopy reveals asymmetric cortical forces in migrating Dictyostelium cells. *Phys Rev Lett* 105(24):248103.
23. Franck C, Maskarinec SA, Tirrell DA, Ravichandran G (2011) Three-dimensional traction force microscopy: A new tool for quantifying cell-matrix interactions. *PLoS ONE* 6(3):e17833.
24. Maskarinec SA, Franck C, Tirrell DA, Ravichandran G (2009) Quantifying cellular traction forces in three dimensions. *Proc Natl Acad Sci USA* 106(52):22108–22113.
25. Hur SS, Zhao Y, Li YS, Botvinick E, Chien S (2009) Live cells exert 3-dimensional traction forces on their substrata. *Cell Mol Bioeng* 2(3):425–436.
26. Legant WR, et al. (2010) Measurement of mechanical tractions exerted by cells in three-dimensional matrices. *Nat Methods* 7(12):969–971.
27. Hansen PC (2001) The L-Curve and its use in the numerical treatment of inverse problems. *Computational Inverse Problems in Electrocardiography* (*Advances in Computational Bioengineering*), ed Johnston PR (WIT Press, Southampton, UK), Vol 5, pp 119-142.
28. Deakin NO, Turner CE (2008) Paxillin comes of age. *J Cell Sci* 121(Pt 15):2435–2444.
29. Bershadsky A, Kozlov M, Geiger B (2006) Adhesion-mediated mechanosensitivity: A time to experiment, and a time to theorize. *Curr Opin Cell Biol* 18(5):472–481.
30. Dubin-Thaler BJ, Giannone G, Döbereiner HG, Sheetz MP (2004) Nanometer analysis of cell spreading on matrix-coated surfaces reveals two distinct cell states and STEPs. *Biophys J* 86(3):1794–1806.
31. Kanchanawong P, et al. (2010) Nanoscale architecture of integrin-based cell adhesions. *Nature* 468(7323):580–584.
32. Jerison ER, Xu Y, Wilen LA, Dufresne ER (2011) Deformation of an elastic substrate by a three-phase contact line. *Phys Rev Lett* 106(18):186103.
33. Style RW, Dufresne ER (2012) Static wetting on deformable substrates, from liquids to soft solids. *Soft Matter* 8(27):7177–7184.
34. Gardel ML, et al. (2008) Traction stress in focal adhesions correlates biphasically with actin retrograde flow speed. *J Cell Biol* 183(6):999–1005.
35. Wolfenson H, Henis YI, Geiger B, Bershadsky AD (2009) The heel and toe of the cell's foot: A multifaceted approach for understanding the structure and dynamics of focal adhesions. *Cell Motil Cytoskeleton* 66(11):1017–1029.
36. Brown CM, et al. (2006) Probing the integrin-actin linkage using high-resolution protein velocity mapping. *J Cell Sci* 119(Pt 24):5204–5214.
37. Hu K, Ji L, Applegate KT, Danuser G, Waterman-Storer CM (2007) Differential transmission of actin motion within focal adhesions. *Science* 315(5808):111–115.
38. del Rio A, et al. (2009) Stretching single talin rod molecules activates vinculin binding. *Science* 323(5914):638–641.
39. Grashoff C, et al. (2010) Measuring mechanical tension across vinculin reveals regulation of focal adhesion dynamics. *Nature* 466(7303):263–266.
40. Sawada Y, et al. (2006) Force sensing by mechanical extension of the Src family kinase substrate p130Cas. *Cell* 127(5):1015–1026.
41. Alexandrova AY, et al. (2008) Comparative dynamics of retrograde actin flow and focal adhesions: Formation of nascent adhesions triggers transition from fast to slow flow. *PLoS ONE* 3(9):e3234.
42. Choi CK, et al. (2008) Actin and alpha-actinin orchestrate the assembly and maturation of nascent adhesions in a myosin II motor-independent manner. *Nat Cell Biol* 10(9):1039–1050.
43. Chrzanowska-Wodnicka M, Burridge K (1996) Rho-stimulated contractility drives the formation of stress fibers and focal adhesions. *J Cell Biol* 133(6):1403–1415.
44. Wolfenson H, et al. (2009) A role for the juxtamembrane cytoplasm in the molecular dynamics of focal adhesions. *PLoS ONE* 4(1):e4304.
45. Zaidel-Bar R, Itzkovitz S, Ma'ayan A, Iyengar R, Geiger B (2007) Functional atlas of the integrin adhesome. *Nat Cell Biol* 9(8):858–867.
46. Zamir E, et al. (1999) Molecular diversity of cell-matrix adhesions. *J Cell Sci* 112(Pt 11):1655–1669.
47. Grinnell F (2003) Fibroblast biology in three-dimensional collagen matrices. *Trends Cell Biol* 13(5):264–269.
48. Xu K, Babcock HP, Zhuang X (2012) Dual-objective STORM reveals three-dimensional filament organization in the actin cytoskeleton. *Nat Methods* 9(2):185–188.
49. DuFort CC, Paszek MJ, Weaver VM (2011) Balancing forces: Architectural control of mechanotransduction. *Nat Rev Mol Cell Biol* 12(5):308–319.
50. Friedl P, Wolf K (2010) Plasticity of cell migration: A multiscale tuning model. *J Cell Biol* 188(1):11–19.
51. Lauffenburger DA, Horwitz AF (1996) Cell migration: A physically integrated molecular process. *Cell* 84(3):359–369.
52. Chen CS (2008) Mechanotransduction – A field pulling together? *J Cell Sci* 121(Pt 20):3285–3292.
53. Barnhart EL, Lee KC, Keren K, Mogilner A, Theriot JA (2011) An adhesion-dependent switch between mechanisms that determine motile cell shape. *PLoS Biol* 9(5):e1001059.
54. Pelham RJ, Jr., Wang Y (1999) High resolution detection of mechanical forces exerted by locomoting fibroblasts on the substrate. *Mol Biol Cell* 10(4):935–945.
55. Klein EA, Yung Y, Castagnino P, Kothapalli D, Assoian RK (2007) Cell adhesion, cellular tension, and cell cycle control. *Methods Enzymol* 426:155–175.
56. Shaner NC, et al. (2008) Improving the photostability of bright monomeric orange and red fluorescent proteins. *Nat Methods* 5(6):545–551.
57. Miller JS, et al. (2010) Bioactive hydrogels made from step-growth derived PEG-peptide macromers. *Biomaterials* 31(13):3736–3743.
58. Shao L, Kner P, Rego EH, Gustafsson MG (2011) Super-resolution 3D microscopy of live whole cells using structured illumination. *Nat Methods* 8(12):1044–1046.
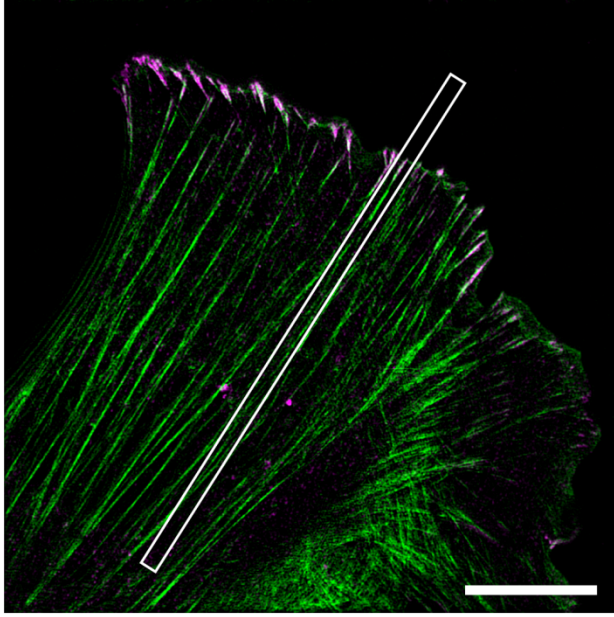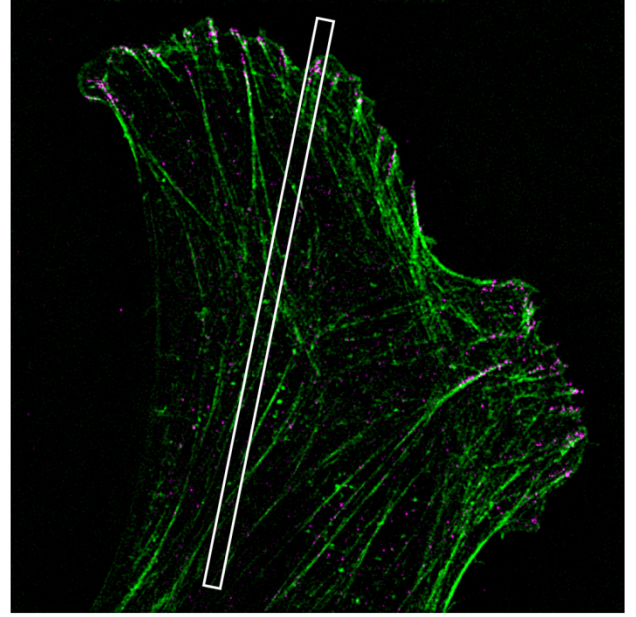
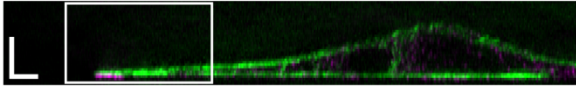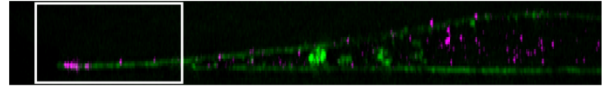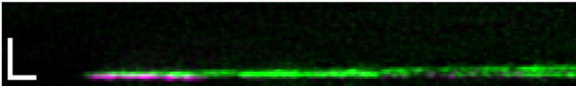**Fig. S1: Super-resolution structured illumination microscopy (SIM) of focal adhesions and actin stress fibers.** (A) A single plane SIM micrograph of a MEF cultured on a 6500 Pa PEG hydrogel and stained for vinculin (magenta) and F-actin (green). Scale bar, 10 μm. (B) Side-view of the inset outlined in (A) showing the thickness of the cell. Spread cell is flat, and significant height increase is observed only near the nucleus. Scale bars, 3 μm for vertical z-axis and 2 μm for horizontal. (C) Magnified side-view of the inset outlined in (C) showing a vinculin-stained focal adhesion and the associated actin stress fiber at the cell periphery. The adhesion is ~100-150 μm tall, and the height of the cell in this region is ~180-280 μm. Scale bars, 3 μm for vertical z-axis and 0.5 μm for horizontal. (D-F) Similar SIM micrographs of a MEF cultured on a 6500 Pa PEG hydrogel and stained for paxillin (magenta) and F-actin (green).
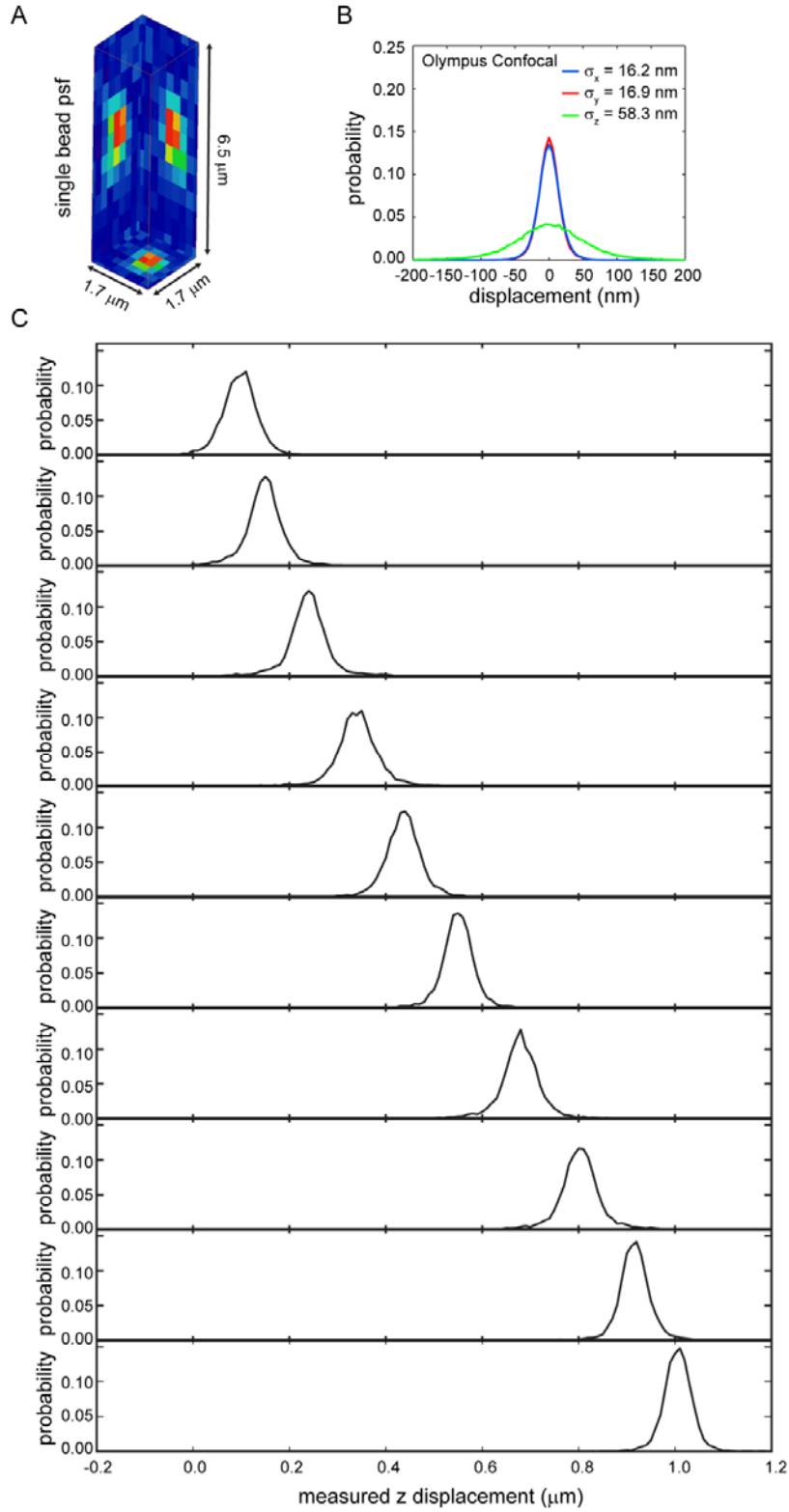
Fig. S2: Bead localization and tracking. (A) Orthogonal axis maximum intensity projection of a single fluorescent bead as acquired in our system. The bead PSF spans approximately 6 pixels in both lateral and axial directions. (B) Probability density function of the measured bead displacements for 100 μm x 100 μm x 5 μm cell free regions of the hydrogel. 10 sequential volumetric images were acquired and the resulting bead displacements (~7000 beads for each acquisition) computed. The standard deviations of these displacements thus represent the aggregate errors from localization, tracking and drift correction. (C) Probability density functions of the z displacements for 10 sequential volumes acquired at 100 nm intervals. 100 μm x 100 μm x 5 μm cell free regions of the hydrogel were acquired sequentially with the center point of each volume shifted in 100 nm increments. The bead tracking algorithm is clearly able to delineate between increments of this size even over a large volume of acquisition.

2
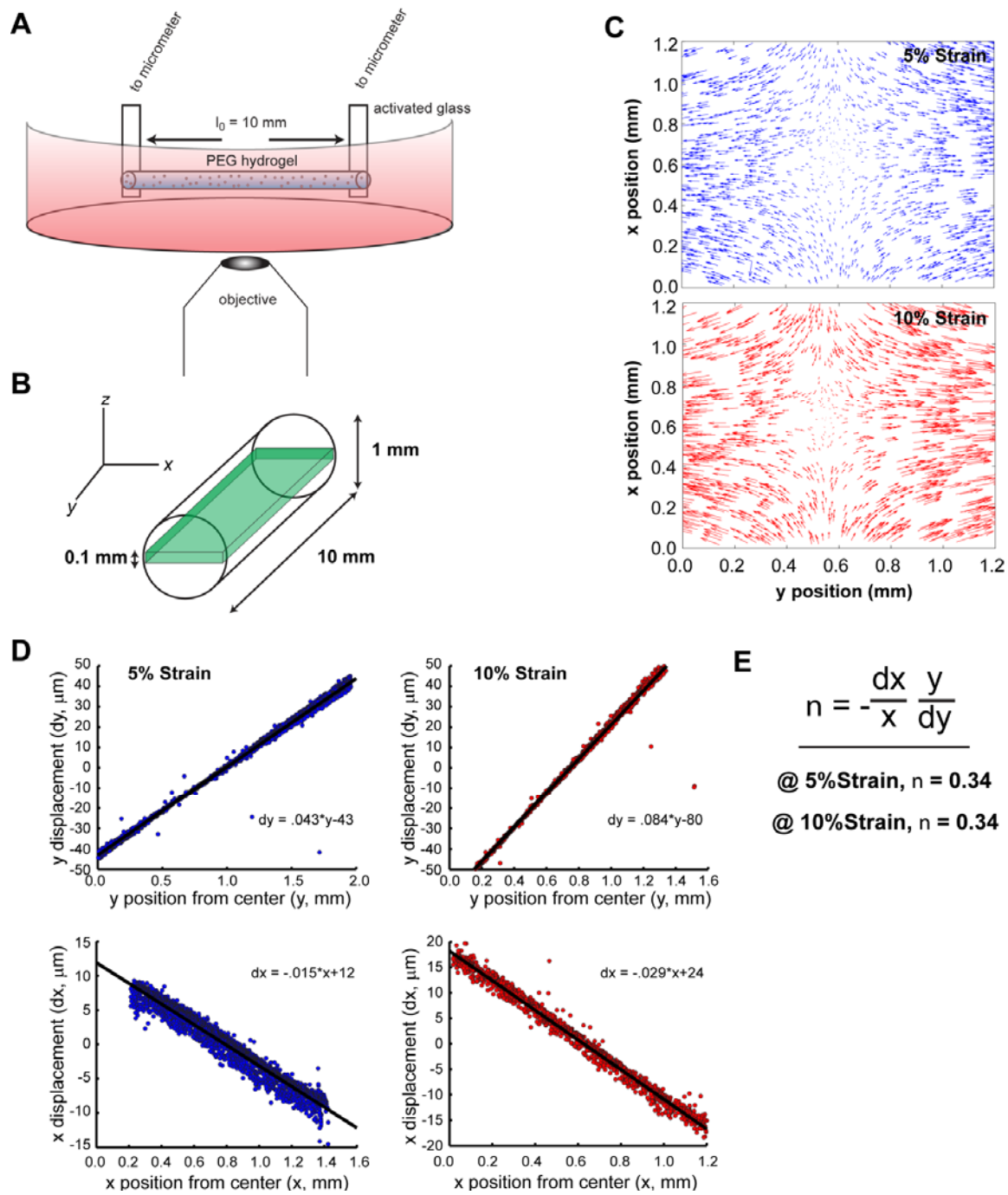
Fig. S3: Measurement of the Poisson ratio. (A) Experimental setup showing PEG hydrogel cylinder suspended above a microscope objective. Cylinders laden with fluorescent beads were cast within PDMS molds, polymerized and allowed to swell overnight. After swelling, the ends of the cylinder were glued to silanized glass slides using additional PEG prepolymer. The glass slides were then attached a micrometer which was mounted above the microscope objective. The entire hydrogel was immersed in PBS for the duration of the experiment. From a resting length of 10 mm, the cylinder was stretched for 5% (10.5 mm) and 10% (11 mm) strain. After each stretch, the hydrogel was allowed to re-equilibrate for 30 minutes to allow for any viscoelastic relaxation. (B) Z-stacks were acquired for the entire thickness of the hydrogel at each strain (stretched along the y axis); however, because system was mounted on a widefield microscope (as opposed to a confocal), three-dimensional tracking was not able to be performed. Instead, a maximum intensity projection was taken from the central 0.1 mm of the cylinder and the 2D bead displacements were tracked. (C) Vector plots showing the bead displacements at both 5 and 10% strain. (D) Scatter plots of the x and y displacement as a function of x and y position (as measured from the centerline of the cylinder) respectively. Linear fits to each dataset, along with fitting parameters are indicated. (E) Poisson ratio ν is estimated from the slopes in (D). Both 5 and 10% strains report a Poisson ratio of 0.34.

3
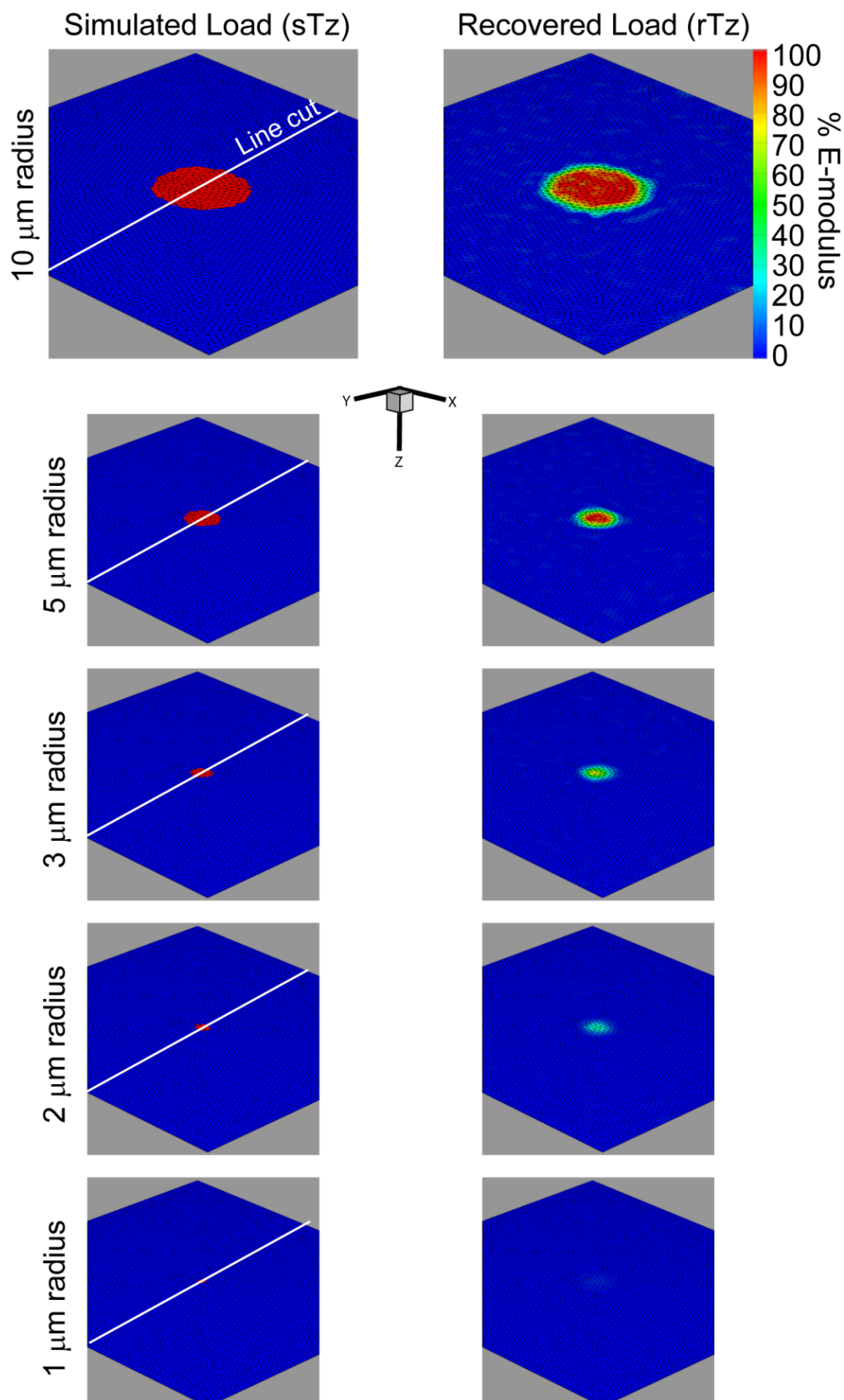
Fig. S4: Overview of the simulated point-like tractions used for resolution and sensitivity analysis. Contour maps showing the simulated tractions, distributed over a circular area of progressively decreasing radius and applied along the z-axis (sTz – simulated traction, z component). For each condition, the recovered tractions (recovered under experimentally relevant levels of bead density and measurement noise) are also shown (rTz – recovered traction, z component). The line plot used in figures S5-S7 is indicated.
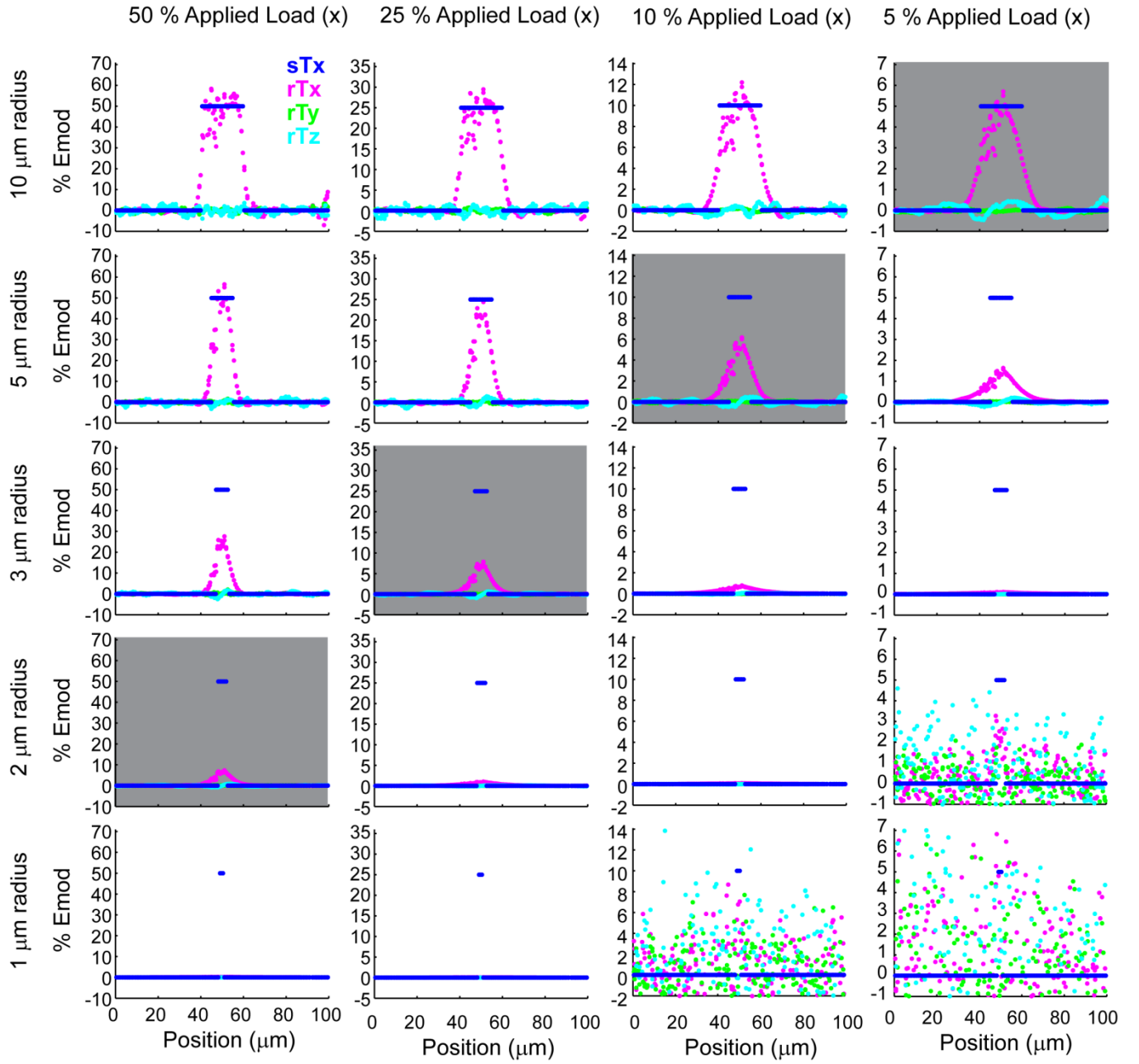
Fig. S5: Numerical characterization of the sensitivity and spatial resolution of point-like traction measurements along the x Cartesian direction. Line cuts are plotted for simulated tractions applied along the x-Cartesian direction (sTx) with decreasing magnitude (50%-5% of the hydrogel elastic modulus) and distributed over a circular area of decreasing radius (10 μm to 1 μm). For each loading, the recovered traction components along each Cartesian direction are plotted (rTx, rTy, rTz). Grey boxes indicate conditions that would be difficult to distinguish under the limits of our system.

5
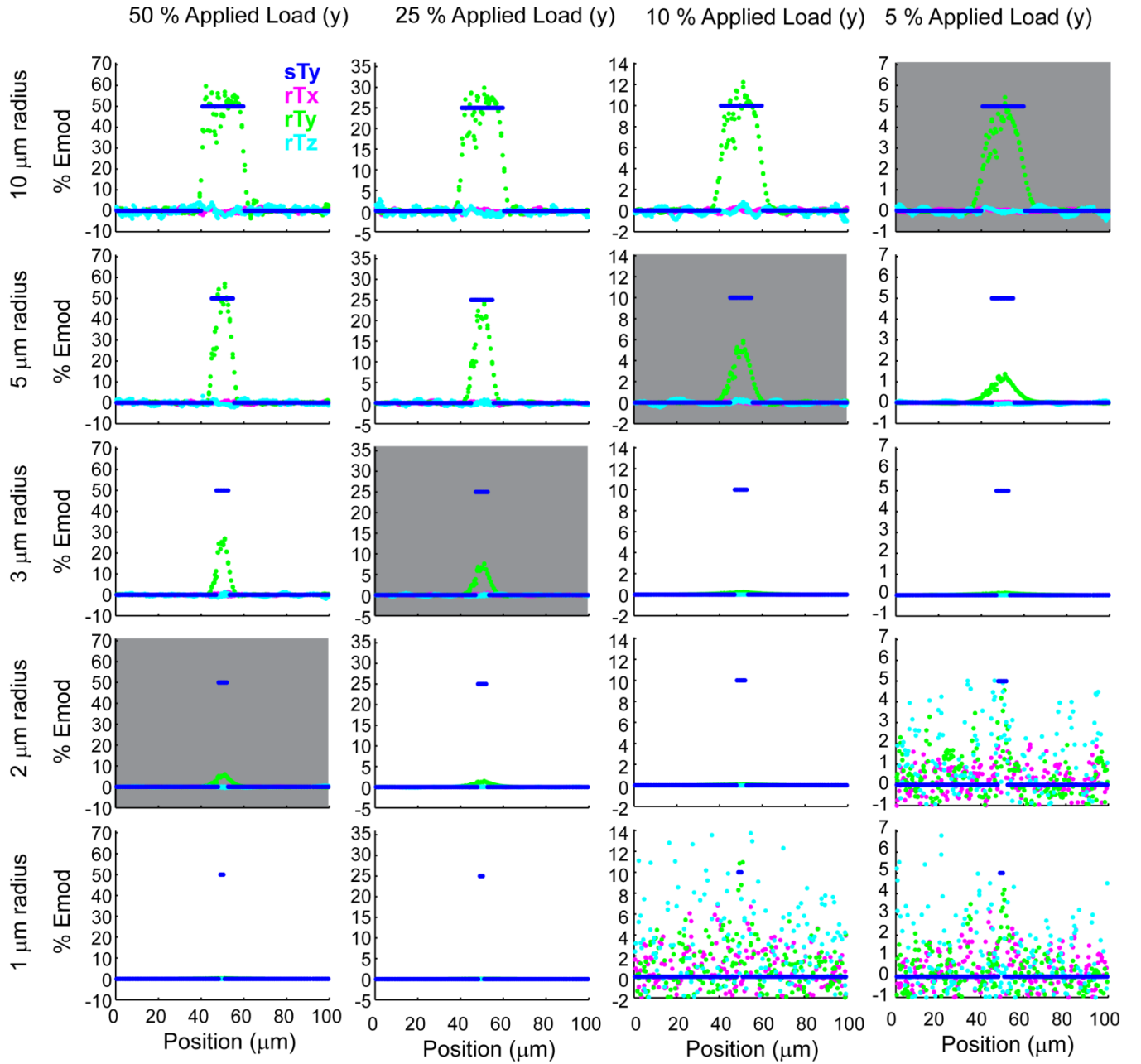
Fig. S6: Numerical characterization of the sensitivity and spatial resolution of point-like traction measurements along the y Cartesian direction. Line cuts are plotted for simulated tractions applied along the y-Cartesian direction (sTy) with decreasing magnitude (50%-5% of the hydrogel elastic modulus) and distributed over a circular area of decreasing radius (10 μm to 1 μm). For each loading, the recovered traction components along each Cartesian direction are plotted (rTx, rTy, rTz). Grey boxes indicate conditions that would be difficult to distinguish under the limits of our system.
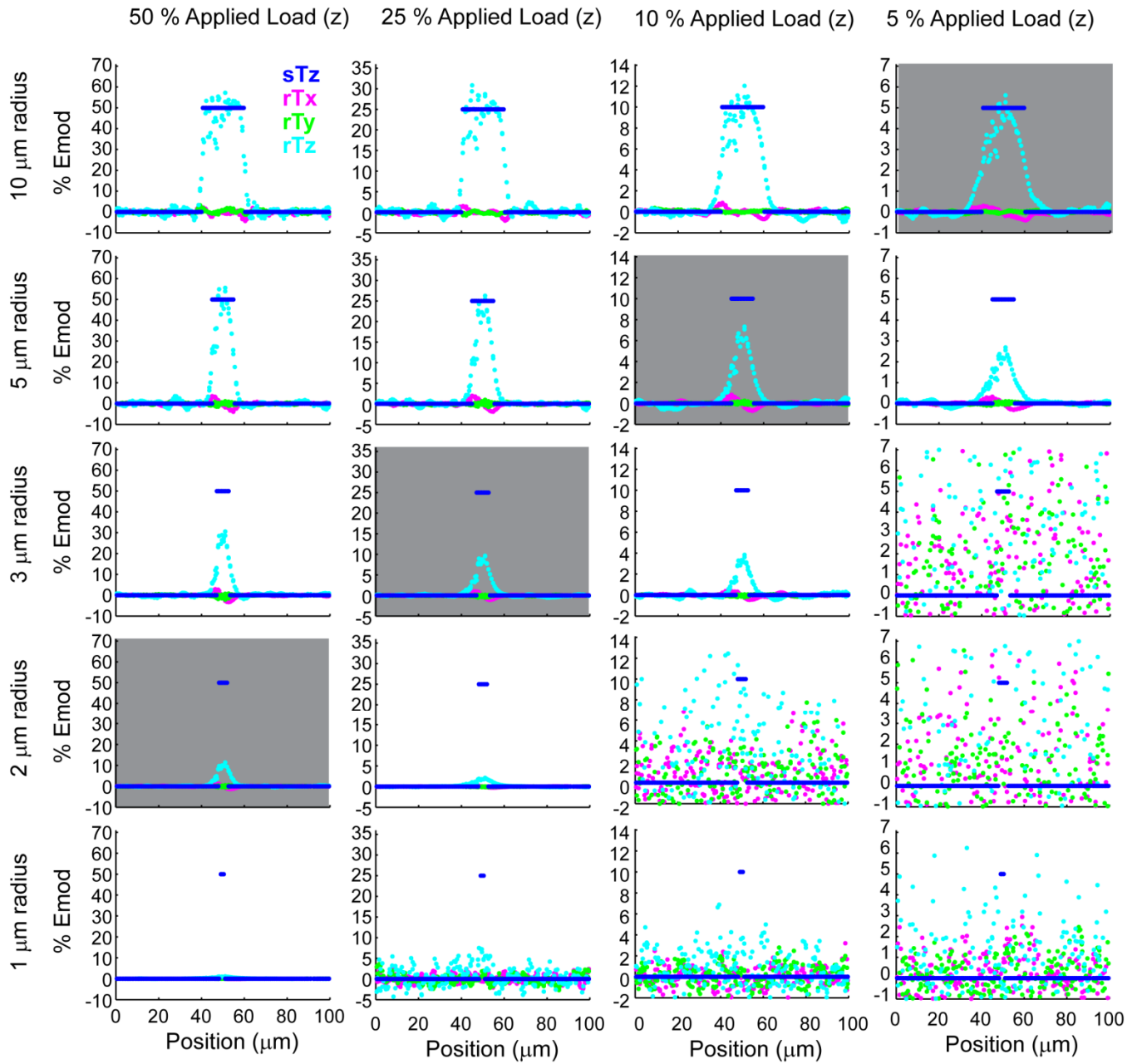
Fig. S7: Numerical characterization of the sensitivity and spatial resolution of point-like traction measurements along the z Cartesian direction. Line cuts are plotted for simulated tractions applied along the z-Cartesian direction (sTz) with decreasing magnitude (50%-5% of the hydrogel elastic modulus) and distributed over a circular area of decreasing radius (10 μm to 1 μm). For each loading, the recovered traction components along each Cartesian direction are plotted (rTx, rTy, rTz). Grey boxes indicate conditions that would be difficult to distinguish under the limits of our system.
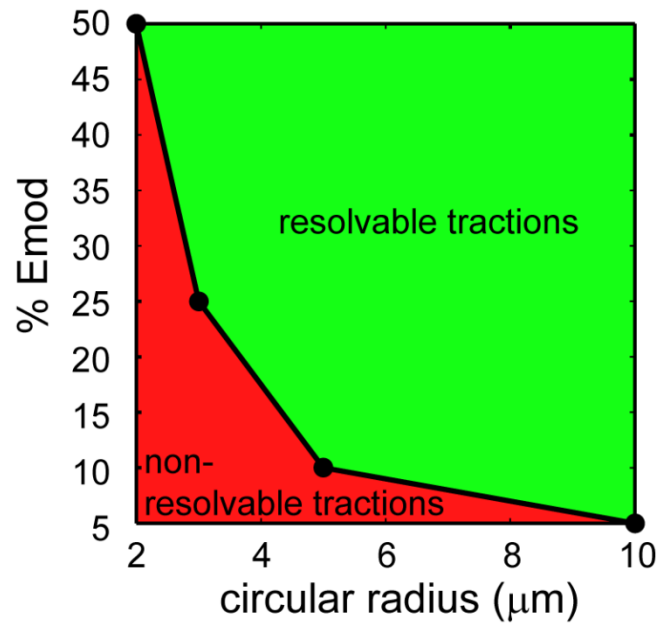
Fig. S8: Diagram of sensitivity vs. resolution for point-like tractions. Plot of the sensitivity (surface tractions expressed as a % elastic modulus (Emod)) vs. spatial resolution (circular radius over which the tractions are distributed). Note that a traction of 25% Emod distributed over a circular region of 3 μm will be resolved by our system, but the peak value will be under reported to be approximately 10% Emod (as illustrated in plots **S5-S7**).
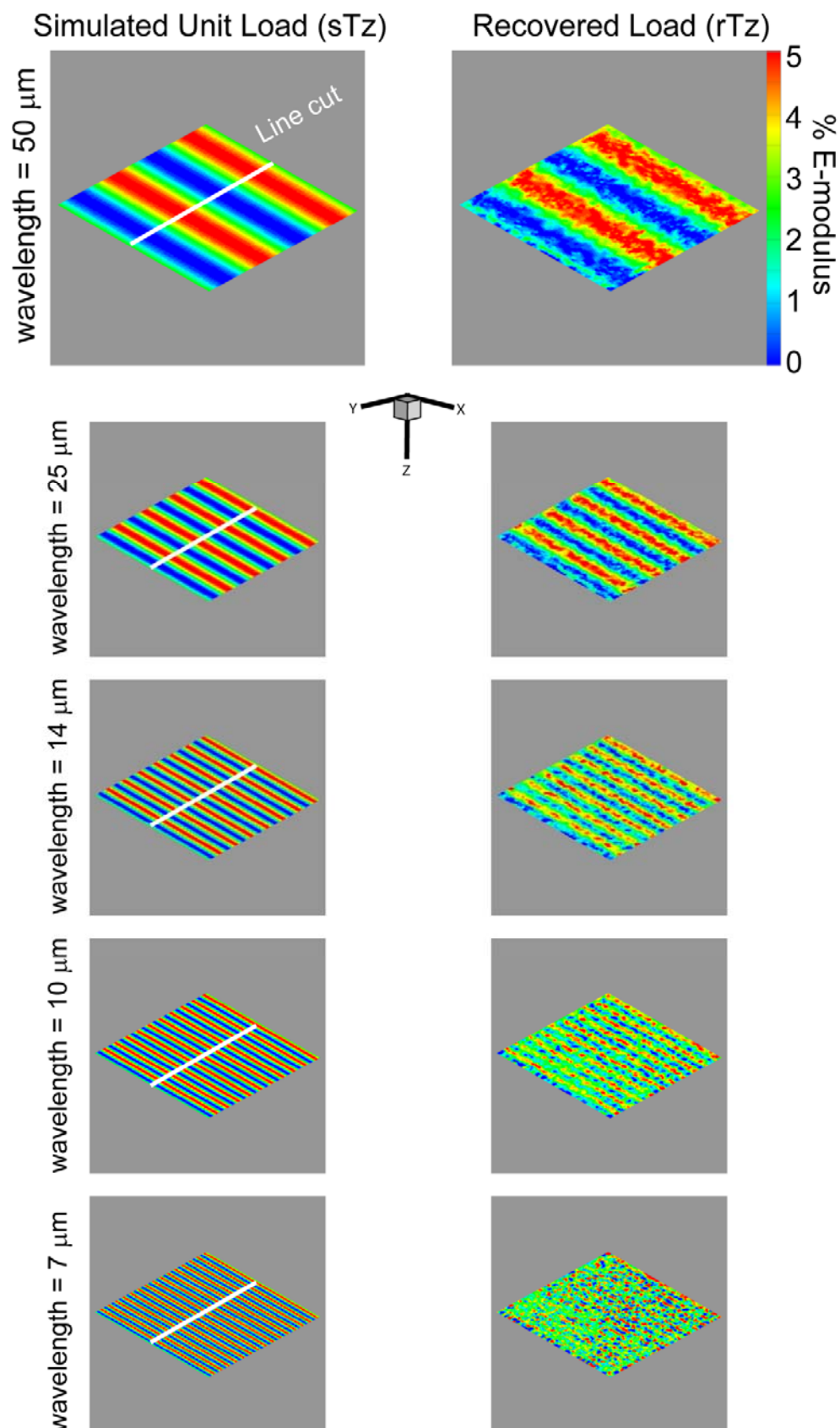
Fig. S9: Overview of the simulated sinusoidal tractions used for resolution and sensitivity analysis. Contour maps showing the simulated tractions, oriented in the z Cartesian direction and distributed over the entire measurement surface with progressively smaller wavelengths. For each condition, the recovered tractions (recovered under experimentally relevant levels of bead density and measurement noise) are also shown (rTz – recovered traction, z component). The line plot used in figures S11-S12 is indicated.
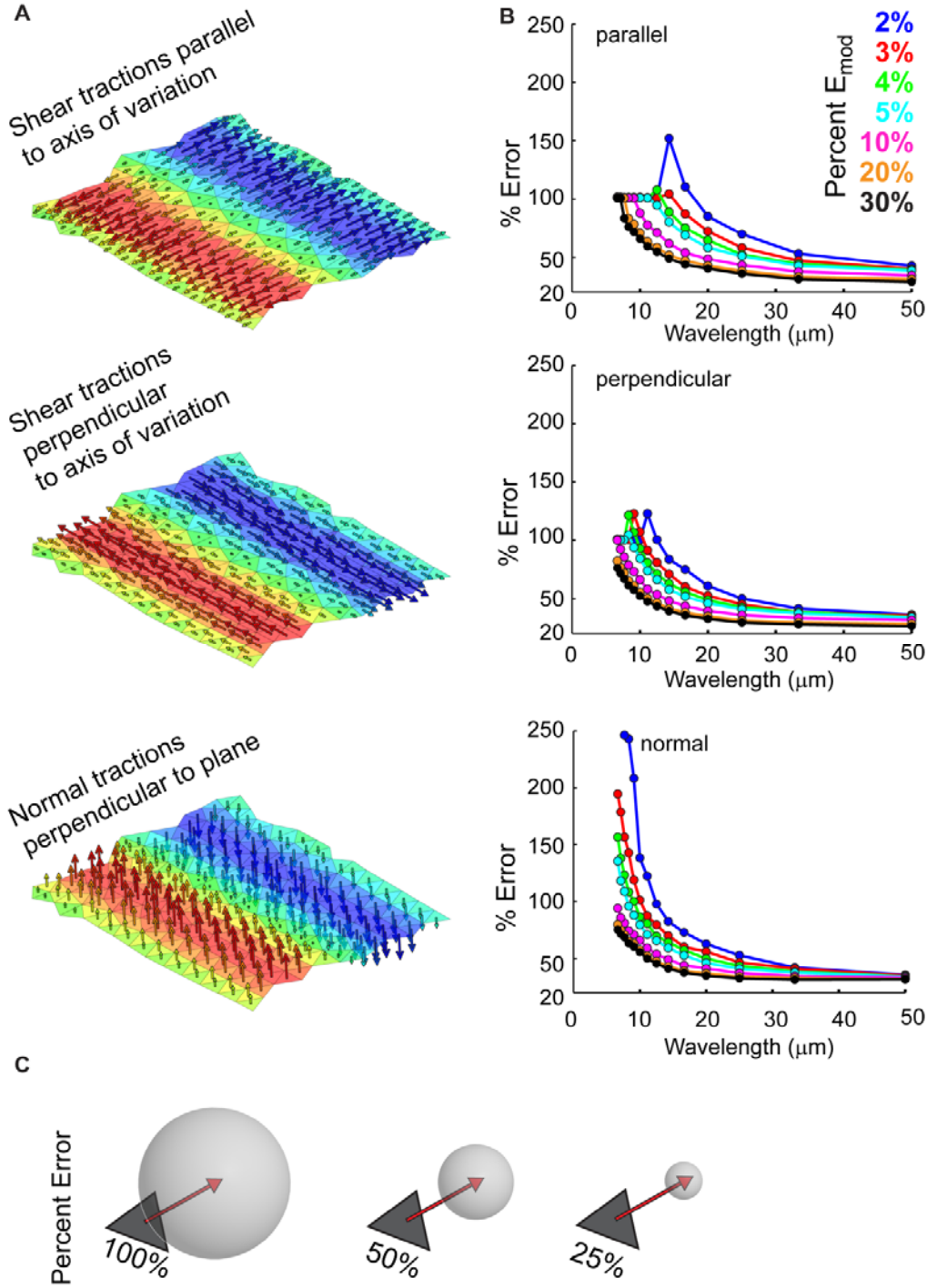
Fig S10: Description of the different orientations used for the simulated sinusoidal loads and global error analysis. (A) The vector valued traction distribution can be decomposed into scalar valued function multiplied by basis vectors. We chose the traditional basis vectors to be aligned with the Cartesian axis except that we rotated them such that the in-plane basis vectors were aligned parallel and perpendicular with the direction of wave propagation. In order to fully characterize the TFM response, we applied loadings at the hydrogel surface as transverse sinusoidal waves of three types: 1) Shear loads in which the direction of force application was orientated perpendicular to the direction of wave propagation, 2) shear loads in which the direction of force application was oriented parallel to the direction of wave propagation, and 3) normal tractions with the forces oriented into and out of the planar halfspace (B) Percent error expressed as $\% \ traction \ error = \frac{|Ts-Tr|_2}{|Ts|_2} \times 100$ of the recovered tractions is plotted as a function of wavelength of the applied loadings for each of the orientations shown in (A). All values were computed for experimentally relevant levels of bead density and displacement measurement error. (C) A graphical depiction of the errors as presented in (B). An error of 25% indicates that the recovered traction vector will lie within a sphere centered at the tip of the simulated traction vector with a radius that is 25% of the magnitude of Ts. This is the 3D vectorial equivalent to traditional error bars on a 1D plot.

10
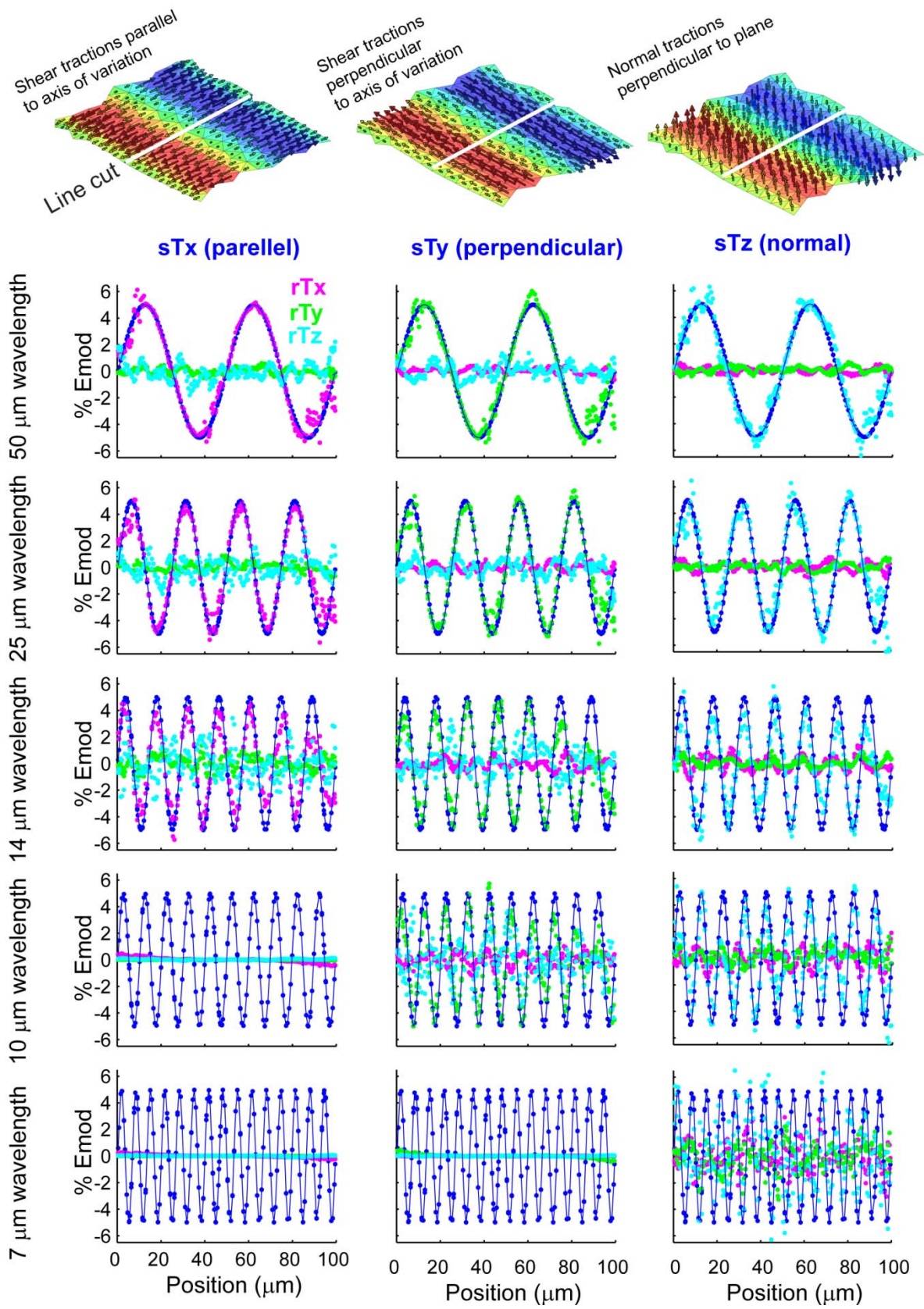
Fig. S11: Numerical characterization of the sensitivity and spatial resolution of oscillating tractions scaled to 5% of the elastic modulus. Line cuts are plotted for simulated tractions applied as parallel shear loads (sTx – parallel), perpendicular shear loads (sTy – perpendicular), or normal loads (sTz - normal), scaled to 5% of the hydrogel elastic modulus. For each loading, the recovered traction components along each Cartesian direction are plotted (rTx, rTy, rTz).

11
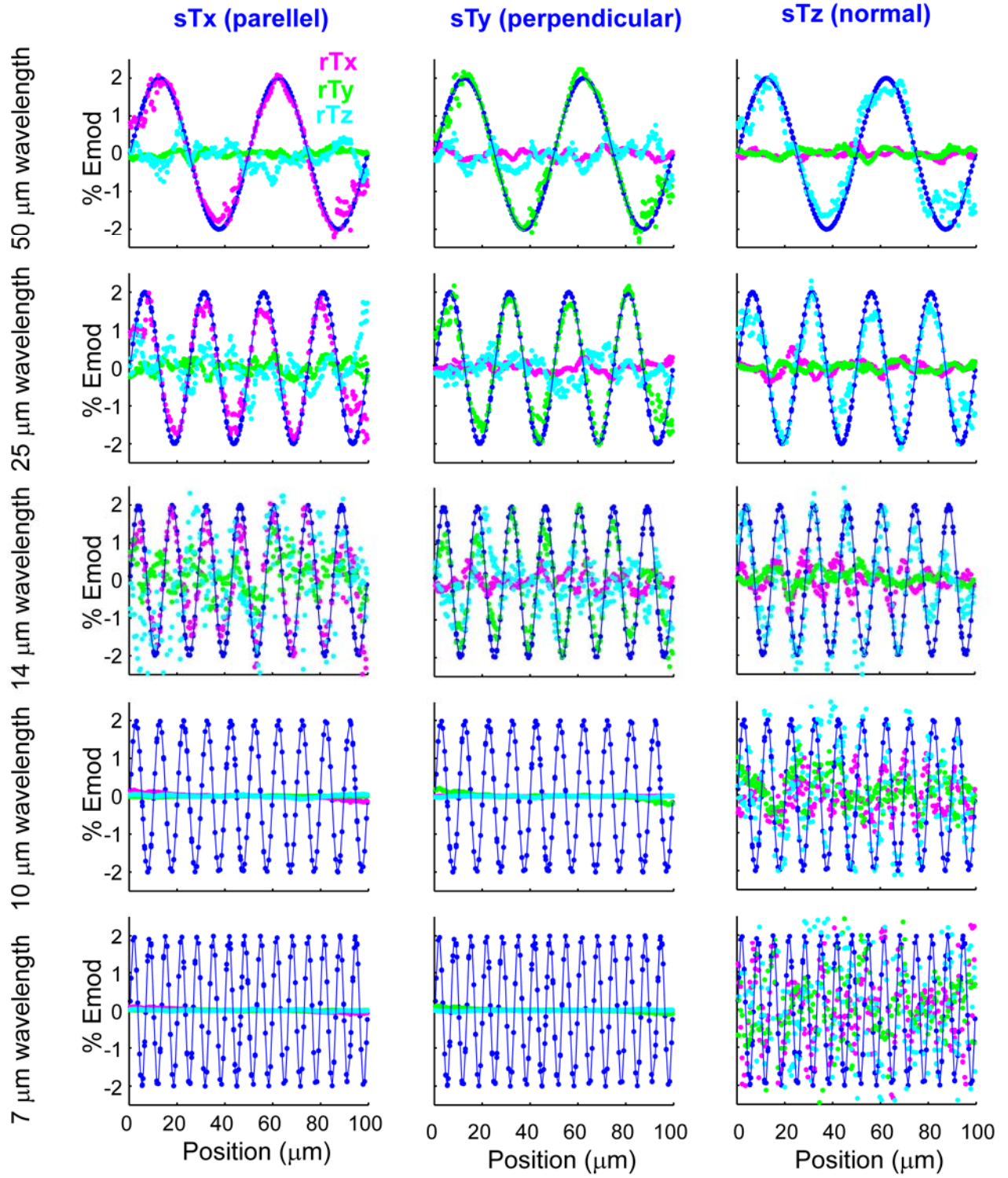
Fig. S12: Numerical characterization of the sensitivity and spatial resolution of oscillating tractions scaled to 2% of the elastic modulus. Line cuts are plotted for simulated tractions applied as parallel shear loads (sTx – parallel), perpendicular shear loads (sTy – perpendicular), or normal loads (sTz - normal), scaled to 2% of the hydrogel elastic modulus. For each loading, the recovered traction components along each Cartesian direction are plotted (rTx, rTy, rTz).
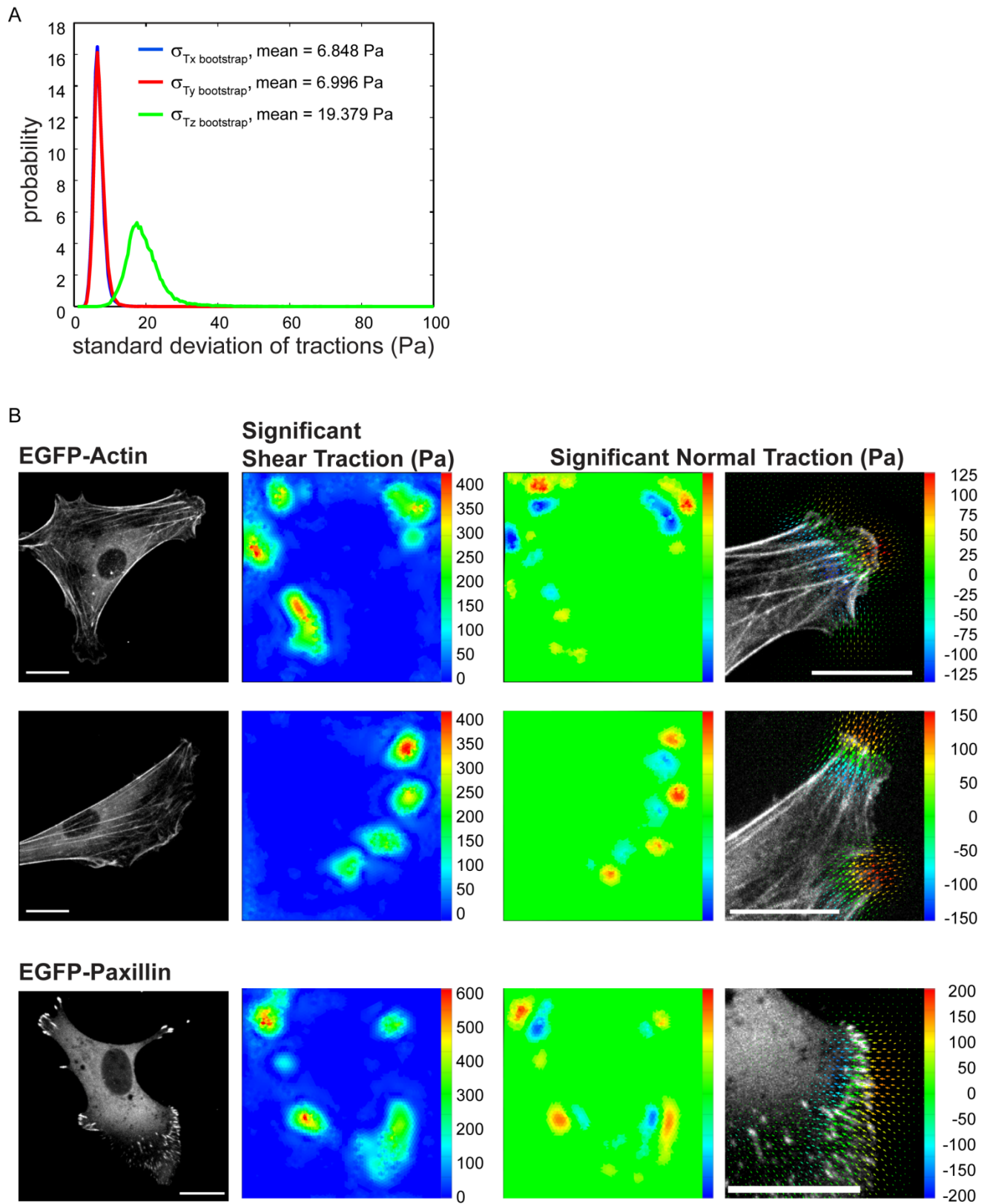
Fig. S13: Bootstrap analysis of recovered tractions. (A) Probability density functions of the standard deviations of the recovered tractions after 100 bootstrap iterations. Data are compiled the three cells shown in (B – 100 measurements each of 33,612 traction vectors). Mean standard deviations of all the recovered traction components in the x, y and z Cartesian directions are indicated. (B) Maximum intensity projections, contour and vector maps of the cells utilized in the bootstrap analysis. For the traction maps, the mean bootstrap values at each facet are plotted (and considered significant) only if each component is above 2X the standard deviations indicated in (A). All scale bars = 20 μm. All PEG hydrogels = 6500 Pa.

13
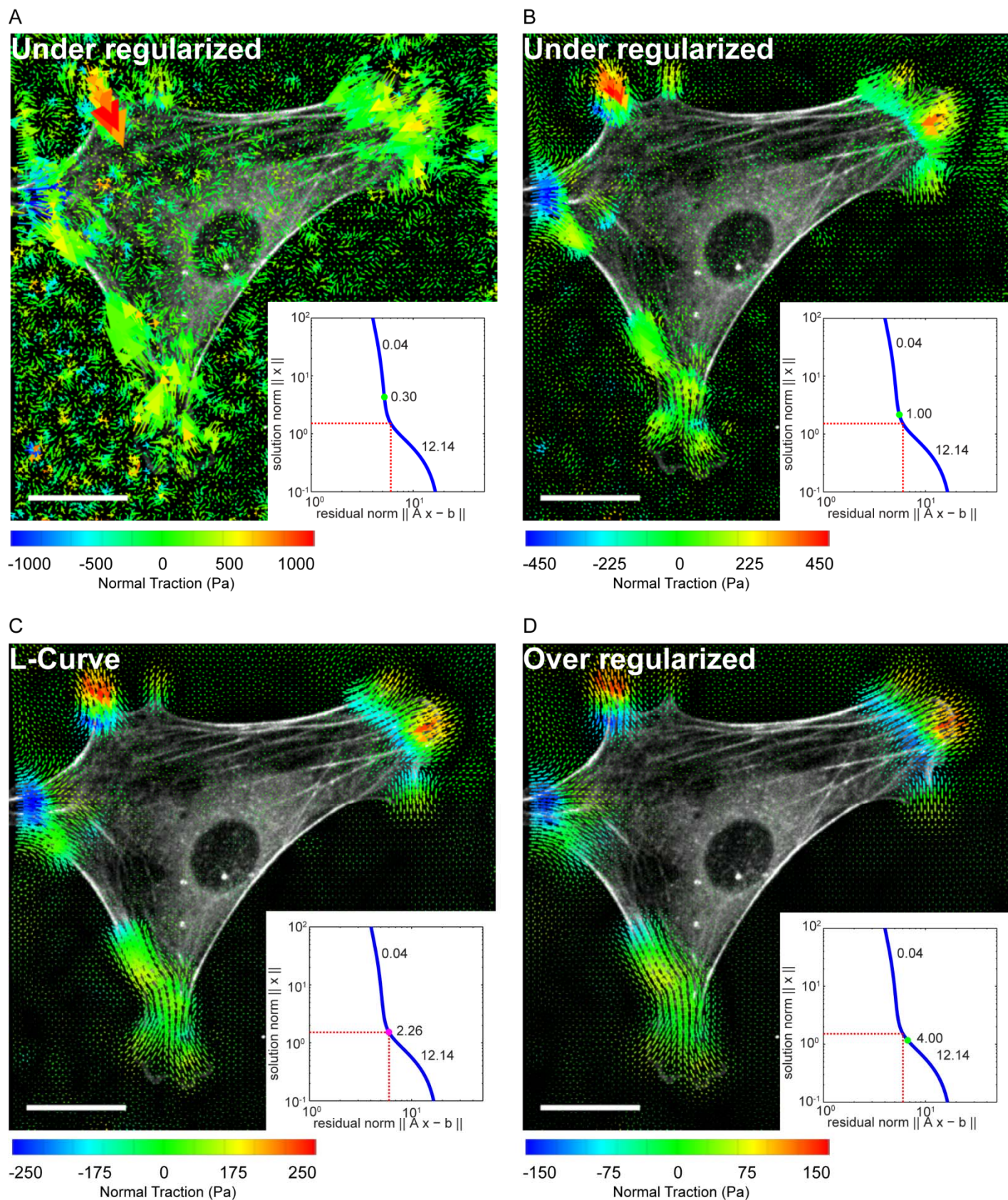
Fig. S14: The effect of regularization. (A-D) Vector plots showing the effect of varying the regularization parameter (λ^2 in equation 27) by more than 1 order of magnitude within the vicinity of the L-curve. Although the absolute values (and background levels) vary between each condition, the locations and relative differences between shear and normal tractions are consistent. All scale bars = 20 μm. All PEG hydrogels = 6500 Pa.

14

A

Computational Domain

200 μm · 100 μm

Focal adhesion →

60 μm

symmetry plane

ENCASTRE boundary condition
(bottom surface)

B

Focal Adhesion / Uniform Load

→ = surface traction of 3.128 kPa

6 μm · 1 μm

TIE constraint

150 nm

PEG hydrogel: E = 6.517 kPa, ν=0.34
Focal adhesion: E = 2.5 MPa, ν=0.49
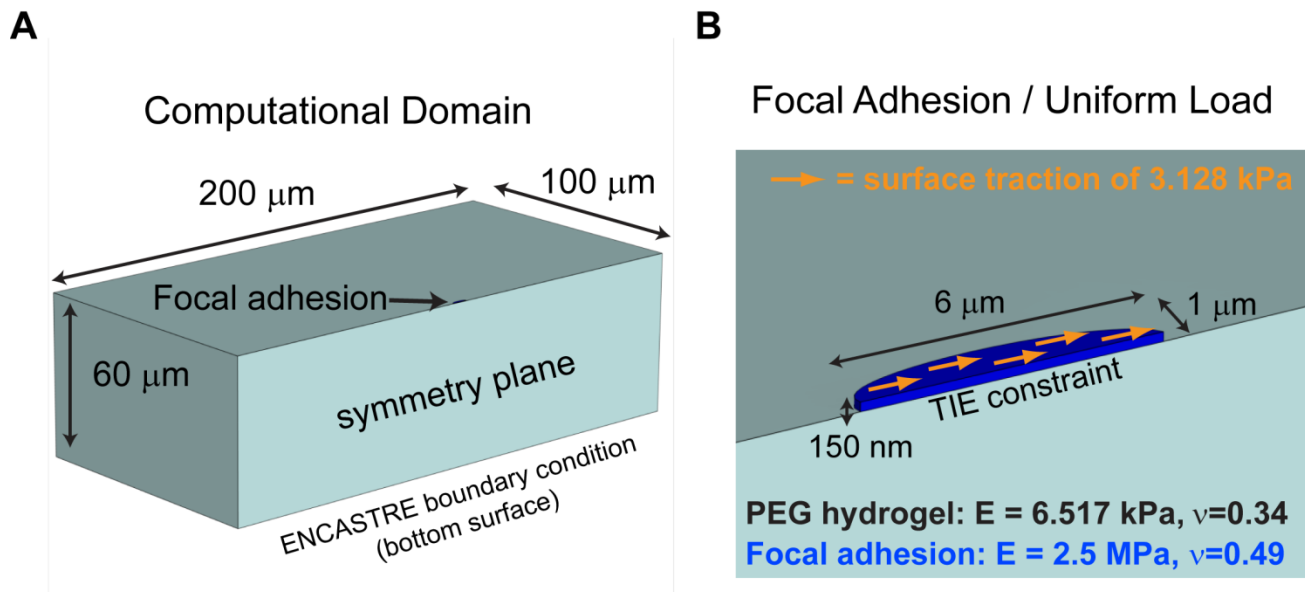
Fig. S15: Dimensions and properties of the finite element simulations (A) The PEG hydrogel was modeled as a 200 x 200 x 60 μm cube with *ENCASTRE boundary conditions along the bottom surface. The material was treated as a NeoHookean solid. All simulations were modeled utilizing a symmetry boundary condition cutting vertically through the center plane of the adhesion. (B) The focal adhesion was modeled as a 150 nm tall elliptical plate with major and minor axis of 6 and 2 μm respectively. These values were comparable to those measured experimentally. The focal adhesion material was treated as linearly elastic with a Young's modulus of 2.431 MPa (373 times more rigid than the initial modulus of the PEG hydrogel) and a Poisson ratio of 0.49. The bottom surface of the adhesion was tied to the PEG hydrogel using the surface to surface *TIE constraint in Abaqus. A shear load was applied to the upper surface of the adhesion using *DSLOAD in Abaqus. The magnitude of this load was increased until the horizontal displacements of the hydrogel matched those observed experimentally. An optimal match for the horizontal displacements was observed for a shear traction of approximately 3.128kPa when distributed uniformly on the dorsal surface of the adhesion.
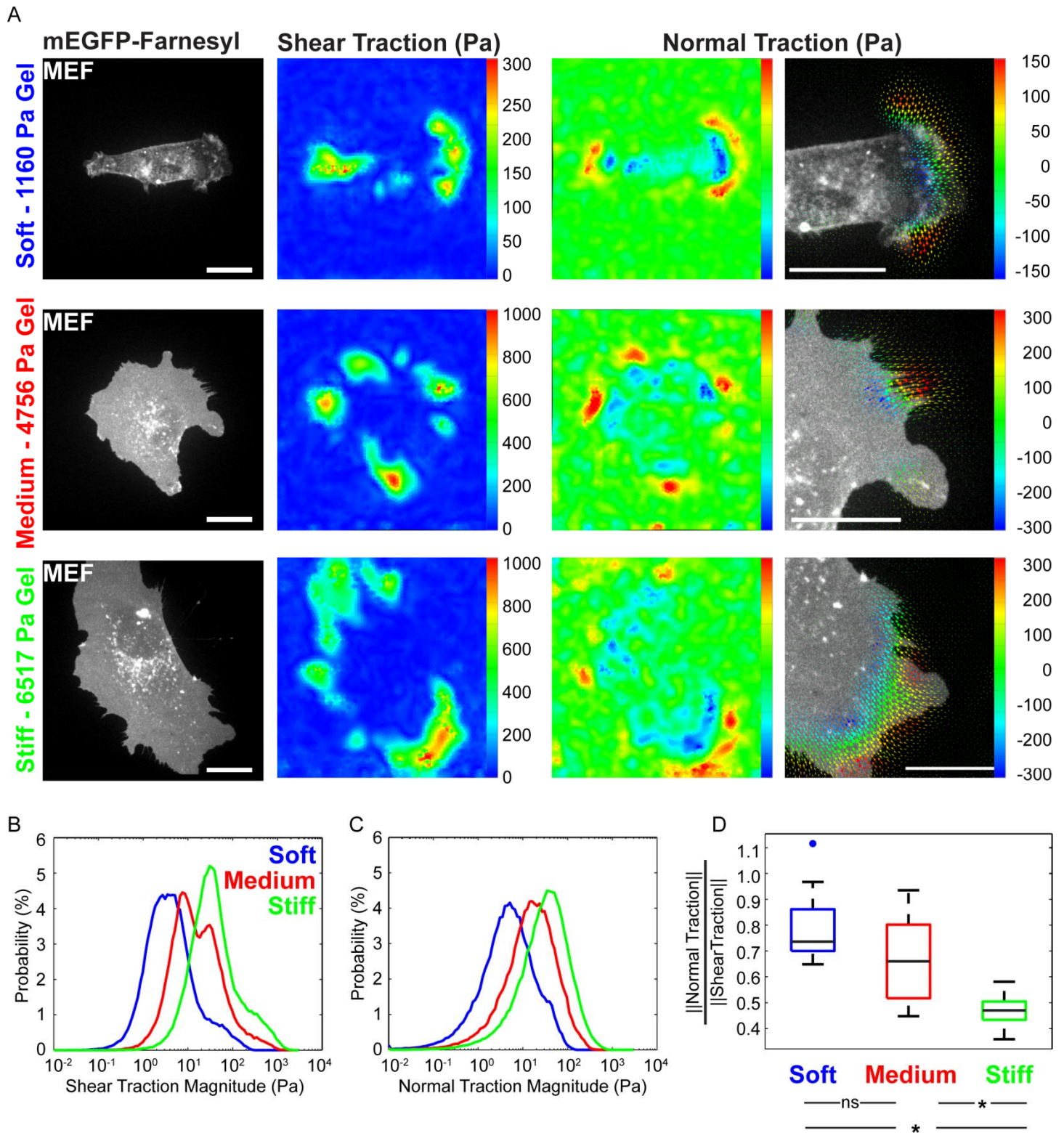
Fig. S16: 2.5D TFM measurements of cells on substrates of varying rigidity. (A) Maximum intensity projections, contour and vector maps of the tractions exerted by representative mEGFP-farnesyl expressing MEFSs cultured on soft (~1kPa), medium (~4.7 kPa) and stiff (~6.5 kPa) PEG hydrogels. (B-C) Compiled probability density functions of the shear or normal tractions exerted by cells in each condition. (D) Ratio of total normal to total shear tractions exerted by cells in each condition. Data in B-D are from n=15 (soft), n=12 (medium) and n=14 (stiff) cells from multiple experiments. Each cell consists of 11204 traction vectors. * = alpha ≤ 0.05 and ns = alpha >0.05 via Kruskal–Wallis one-way analysis of variance and Tukey's HSD (Honestly Significant Difference) tests. All scale bars = 20 μm.
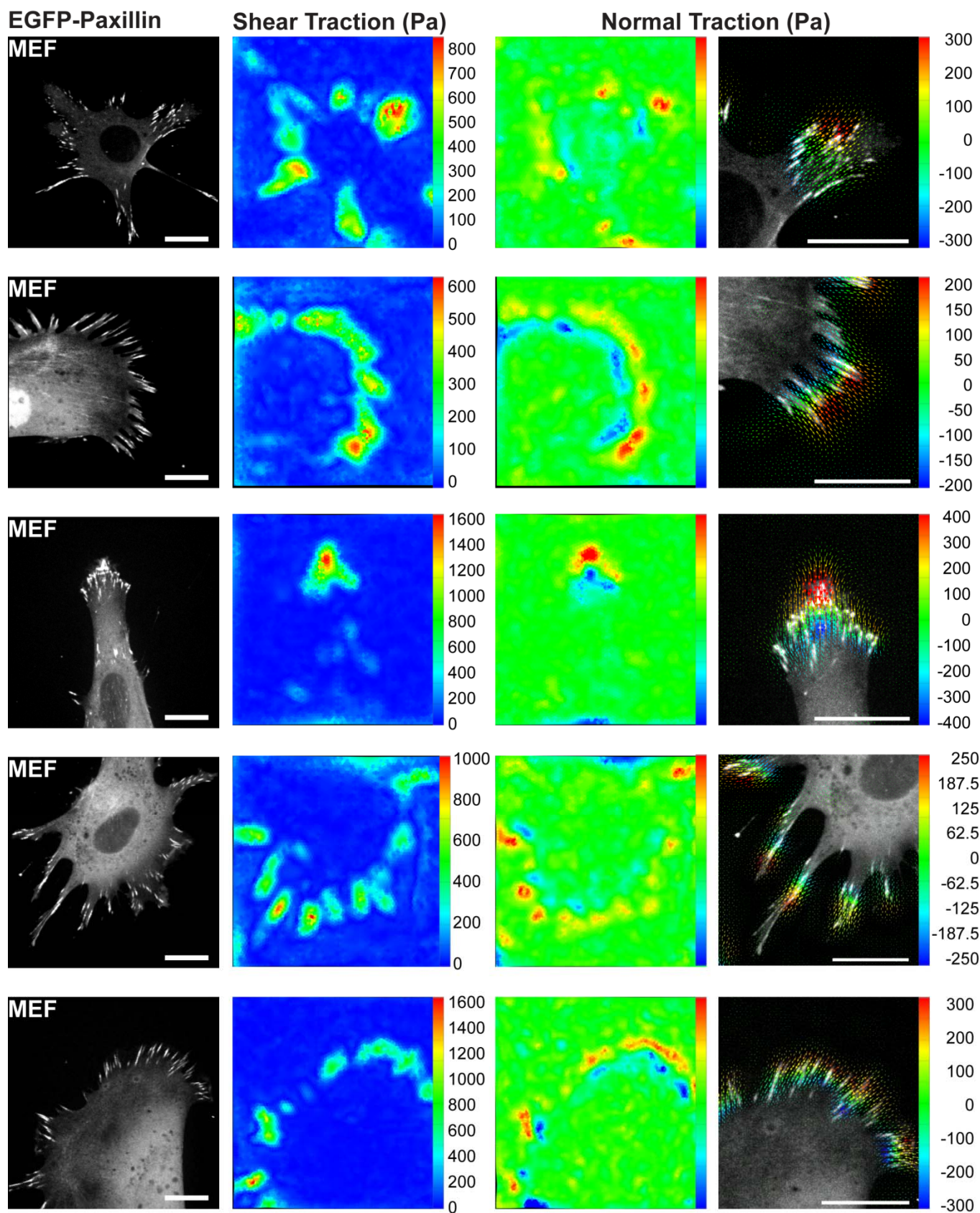
Fig. S17: Representative images and tractions of mouse embryo fibroblasts. Maximum intensity projections, contour and vector maps of the tractions exerted by representative mouse embryo fibroblasts expressing paxillin-EGFP. All scale bars = 20 μm. All PEG hydrogels = 6500 Pa.
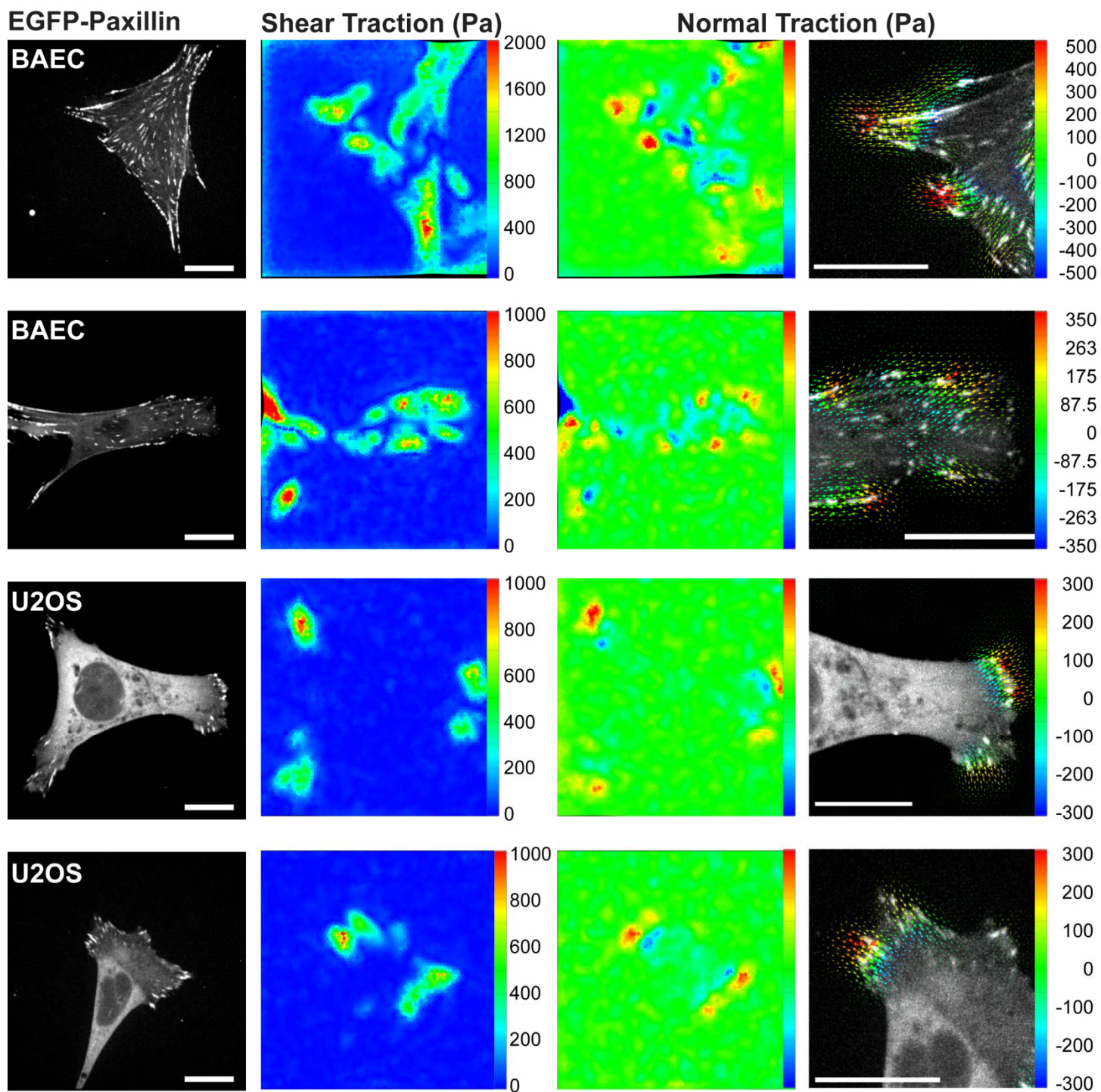
Fig. S18: Representative images and tractions of endothelial and osteosarcoma cells. Maximum intensity projections, contour and vector maps of the tractions exerted by representative bovine aorta endothelial cells and U2OS human osteosarcoma cells expressing Paxillin-EGFP. All scale bars = 20 μm. All PEG hydrogels 6500 Pa.
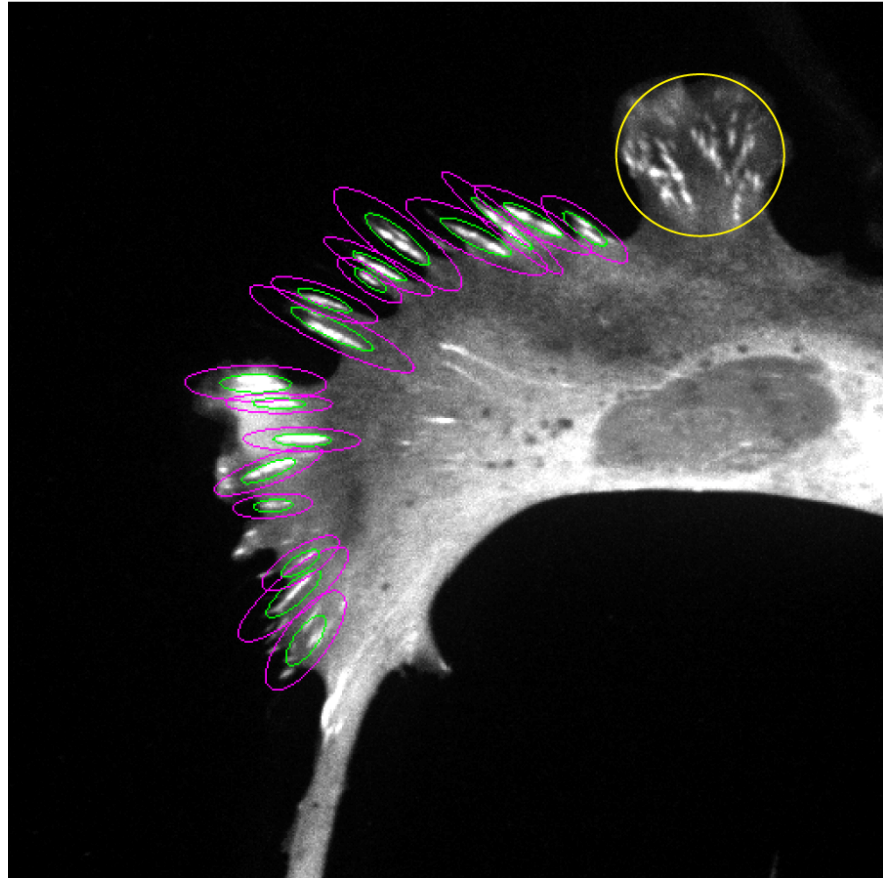
Fig. S19: Focal adhesion segmentation and regions of traction integration. Maximum intensity projection of a representative MEF expressing Paxillin-EGFP. Elongated, peripheral focal adhesions were outlined manually and ellipses fit to each region as detailed in Supplementary Materials. Green ellipses indicate the ellipses fit to each adhesion. Magenta ellipses indicate the expanded regions over which tractions were compiled for each adhesion. The yellow circle highlights small punctuate adhesions that were not included in the analysis.

% E-mod	Stiff 6517 Pa	Medium 4756 Pa	Soft 1160Pa
50	3257	2378	580
25	1629	1189	290
10	652	476	116
5	326	238	58
4	261	190	46
3	196	143	35
2	130	95	23

Table S1: Values of elastic moduli of PEG hydrogels scaled by % Emod as used in resolution and sensitivity analysis.

Supplementary Methods and Discussion:

Bead localization, tracking and noise measurement

In order to measure the displacement field within the hydrogel, we tracked the movements of sub-diffraction limit 200 nm fluorescent beads physically entrapped within the hydrogel. Because the diameter of the beads is approximately an order of magnitude larger than the pore size of polymerized PEG hydrogels (1), the beads do not diffuse within the hydrogel and thus accurately represent the movement of the substrate. The fluorescent beads make up approximately 0.01% of the substrate volume, therefore incorporation of the beads should minimally impact substrate mechanics at the scale of focal adhesions.

Each volumetric dataset was filtered to remove high frequency noise and local maxima were identified as described in (2, 3). These local maxima represent preliminary bead centroid estimates. For each bead, a 5 x 5 x 5 voxel region surrounding each maxima was isolated in the unfiltered, raw image. The size of this region was chosen to encompass the majority of the bead PSF while not being so large as to increase the probability of having multiple beads in each sub-image (**Figure S2A**). The centroid estimate for the bead within each sub-image was then refined using a 3D Gaussian, maximum likelihood estimator (MLE), where we have adopted the notation described in (4) for fitting a 2D Gaussian. Here, we modify those equations in order to perform 3D Gaussian fitting. The point spread function was modeled as a general 3D Gaussian function according to

$$PSF\ (x,y,z) = \frac{1}{(2\pi)^{\frac{3}{2}}\sigma_x\sigma_y\sigma_z}\ e^{-\left(\frac{x^2}{2\sigma_x^2}+\frac{y^2}{2\sigma_y^2}+\frac{z^2}{2\sigma_z^2}\right)} \qquad (1)$$

The imaging model, which incorporates the effects of finite voxel size is

$$\mu_k(x,y,z) = \theta_I \iiint PSF(u,v,w)du,dv,dw + \theta_{bg} \qquad (2)$$

where $\mu(x,y,z)$ denotes the expected value in the kth pixel, θ_I is the expected photon count, θ_{bg} is the expected background count and du, dv and dw are the length, width and depth of the of the kth voxel respectively. This

model was in turn approximated using error functions and unit voxel dimensions (the localized centroids were scaled by the asymmetric voxel dimensions after fitting) in order to simplify computation as follows

$$\mu_k(x,y,z) = \theta_I \Delta E_x(x,y,z)\Delta E_y(x,y,z)\Delta E_z(x,y,z) \qquad (3)$$

where

$$\Delta E_x(x,y,z) = \frac{1}{2}\left[erf\left(\frac{x-\theta_x+\frac{1}{2}}{\sqrt{2}\sigma_x}\right) - erf\left(\frac{x-\theta_x-\frac{1}{2}}{\sqrt{2}\sigma_x}\right)\right] \qquad (4)$$

$$\Delta E_y(x,y,z) = \frac{1}{2}\left[erf\left(\frac{y-\theta_y+\frac{1}{2}}{\sqrt{2}\sigma_y}\right) - erf\left(\frac{y-\theta_y-\frac{1}{2}}{\sqrt{2}\sigma_y}\right)\right] \qquad (5)$$

$$\Delta E_z(x,y,z) = \frac{1}{2}\left[erf\left(\frac{z-\theta_z+\frac{1}{2}}{\sqrt{2}\sigma_z}\right) - erf\left(\frac{z-\theta_z-\frac{1}{2}}{\sqrt{2}\sigma_z}\right)\right] \qquad (6)$$

and θ_x, θ_y, and θ_z are the expected centroid coordinates. The Gaussian standard deviations of $\sigma_x = 1.25$, $\sigma_y = 1.11$, and $\sigma_z = 1.07$ voxels were determined from the average fits of 10 spatially isolated beads acquired under the same imaging parameters as those used for traction force calculations.

For a Poisson process (which describes the acquisition of images using a CCD camera), the process likelihood is given by

$$L(\bar{n}|\theta) = \prod_k \frac{\mu_k(x,y,z)^{n_k}e^{-\mu_k(x,y,z)}}{n_k!} \qquad (7)$$

where n_k is the number of photons detected in the kth voxel of the raw image (i.e. not the band pass filtered image), and θ is the parameter set defined by $\{\theta_x, \theta_y, \theta_z, \theta_I, \theta_{bg}\}$. Parameter estimation was carried out via

Newton-Raphson iteration in order to maximize the log likelihood function $\ln\left(L(\bar{n}|\theta)\right)$. As in (4), the iterative updates were computed utilizing the partial derivatives of equation 7 as

$$\frac{\partial\ln\left(L(\bar{n}|\theta)\right)}{\partial\theta_i} = \sum_k \frac{\partial u_k(x,y,z)}{\partial\theta_i}\left(\frac{n_k}{u_k(x,y,z)}-1\right) \qquad \textbf{(8)}$$

The coordinates of the local maxima within each sub-image were used as initial guesses for θ_x, θ_y, and θ_z. The raw image intensity of the peak voxel was used as an initial guess for θ_I and the mode of the isolated sub-image around each bead used as an initial guess for θ_{bg}. After each iteration, the parameter set was updated according to

$$\theta_i \rightarrow \theta_i - \left[\sum_k \frac{\partial u_k(x,y,z)}{\partial\theta_i}\left(\frac{n_k}{u_k(x,y,z)}-1\right)\right] \times \left[\sum_k \frac{\partial^2 u_k(x,y,z)}{\partial\theta_i^2}\left(\frac{n_k}{u_k(x,y,z)}-1\right) - \frac{\partial u_k(x,y,z)^2}{\partial\theta_i}\frac{n_k}{u_k(x,y,z)^2}\right]^{-1} \textbf{(9)}$$

Note the change in sign from equation 13 in (4). For each bead, 20 iterations were performed, which was found to be adequate for algorithm convergence. The partial derivatives required for the Newton-Raphson iteration are as follows:

$$\frac{\partial u_k(x,y,z)}{\partial\theta_x} = \frac{\theta_I}{\sqrt{2\pi}\sigma_x}\left(e^{\frac{-\left(x_k-\theta_x-\frac{1}{2}\right)^2}{2\sigma_x^2}} - e^{\frac{-\left(x_k-\theta_x+\frac{1}{2}\right)^2}{2\sigma_x^2}}\right)\Delta E_y(x,y,z)\Delta E_z(x,y,z) \quad \textbf{(10)}$$

$$\frac{\partial^2 u_k(x,y,z)}{\partial\theta_x^2} = \frac{\theta_I}{\sqrt{2\pi}\sigma_x^3}\left(\left(x_k-\theta_x-\frac{1}{2}\right)e^{\frac{-\left(x_k-\theta_x-\frac{1}{2}\right)^2}{2\sigma_x^2}} - \left(x_k-\theta_x+\frac{1}{2}\right)e^{\frac{-\left(x_k-\theta_x+\frac{1}{2}\right)^2}{2\sigma_x^2}}\right)\Delta E_y(x,y,z)\Delta E_z(x,y,z) \quad \textbf{(11)}$$

$$\frac{\partial u_k(x,y,z)}{\partial\theta_y} = \frac{\theta_I}{\sqrt{2\pi}\sigma_y}\left(e^{\frac{-\left(y_k-\theta_y-\frac{1}{2}\right)^2}{2\sigma_y^2}} - e^{\frac{-\left(y-\theta_y+\frac{1}{2}\right)^2}{2\sigma_y^2}}\right)\Delta E_x(x,y,z)\Delta E_z(x,y,z) \quad \textbf{(12)}$$

$$\frac{\partial^2 u_k(x,y,z)}{\partial \theta_y^2} = \frac{\theta_I}{\sqrt{2\pi}\sigma_y^3}\left(\left(y_k - \theta_y - \frac{1}{2}\right)e^{\frac{-\left(y_k-\theta_y-\frac{1}{2}\right)^2}{2\sigma_y^2}} - \left(y_k - \theta_y + \frac{1}{2}\right)e^{\frac{-\left(y-\theta_y+\frac{1}{2}\right)^2}{2\sigma_y^2}}\right)\Delta E_x(x,y,z)\Delta E_z(x,y,z) \quad \textbf{(13)}$$

$$\frac{\partial u_k(x,y,z)}{\partial \theta_z} = \frac{\theta_I}{\sqrt{2\pi}\sigma_z}\left(e^{\frac{-\left(z_k-\theta_z-\frac{1}{2}\right)^2}{2\sigma_z^2}} e^{\frac{-\left(z_k-\theta_z+\frac{1}{2}\right)^2}{2\sigma_z^2}}\right)\Delta E_x(x,y,z)\Delta E_y(x,y,z) \quad \textbf{(14)}$$

$$\frac{\partial^2 u_k(x,y,z)}{\partial \theta_z^2} = \frac{\theta_I}{\sqrt{2\pi}\sigma_z^3}\left(\left(z_k - \theta_z - \frac{1}{2}\right)e^{\frac{-\left(z_k-\theta_z-\frac{1}{2}\right)^2}{2\sigma_z^2}} - \left(z_k - \theta_z + \frac{1}{2}\right)e^{\frac{-\left(z_k-\theta_z+\frac{1}{2}\right)^2}{2\sigma_z^2}}\right)\Delta E_x(x,y,z)\Delta E_z(x,y,z) \quad \textbf{(15)}$$

$$\frac{\partial u_k(x,y,z)}{\partial \theta_I} = \Delta E_x(x,y,z)\Delta E_y(x,y,z)\Delta E_z(x,y,z) \quad \textbf{(16)}$$

$$\frac{\partial^2 u_k(x,y,z)}{\partial \theta_I^2} = 0 \quad \textbf{(17)}$$

$$\frac{\partial u_k(x,y,z)}{\partial \theta_{bg}} = 1 \quad \textbf{(18)}$$

$$\frac{\partial^2 u_k(x,y,z)}{\partial \theta_{bg}^2} = 0 \quad \textbf{(19)}$$

Once the bead centroid within each sub-image was identified, this value was scaled according to the experimental voxel dimensions and registered to the original image coordinates. Displacement trajectories between the stressed (i.e. subject to cell generated tractions) and relaxed (after SDS treatment) datasets were computed according to a local pattern matching algorithm defined in detail in (5). To correct for mechanical drift, regions of the hydrogel that were significantly far from the cell were indicated by the user in each dataset. The displacement of these beads should be only affected by mechanical drift and not by cell generated tractions, thus the mean displacement of beads in these regions was used to correct for drift in the rest of the dataset.

Because errors in the measured experimental displacements will be a combination of bead centroid localization, bead tracking precision, and our ability to correct for any experimental drift or swelling within the hydrogel volume, we experimentally measured the aggregate of these factors by sequentially measuring the displacement field in cell-free regions of the hydrogel. Ten sequential 20 μm thick stacks (41 image slices each) were acquired under conditions identical to those used for traction calculation. Displacement trajectories within each of these stacks were computed and the standard deviations of these displacements used to describe the experimental errors. In order to correct for experimental drift, the mean value of all displacements in each of the Cartesian direction was subtracted from each measurement. The displacement errors in each of the three Cartesian directions obtained on the Olympus confocal were normally distributed about zero with standard deviations of 16.2, 16.9 and 58.3 nm for the x, y, and z directions respectively (**Figure S2B**). Measurements obtained on the Zeiss confocal had slightly lower standard deviations of 17.2, 11, and 35 nm in the x, y and z directions. The asymmetry of the errors in x and y is likely the result of a slight shift within the sample during the acquisition process.

To confirm that our bead tracking algorithm could accurately discern displacements of the order of those reported experimentally, we acquired 11, 20 μm thick confocal image stacks with center positions shifted by increments of 100 nm on the Olympus confocal. In each of these datasets, our algorithm accurately reported the mean z translation with a measurement spread comparable to that observed for the static measurements (i.e. ~58nm, **Figure S2C**). Because the displacement errors for the lateral directions are ~3X smaller than for the axial direction, we anticipate the ability to resolve even finer displacements in these directions, although the precision of our x-y microscope stage was not sufficient to test this experimentally.

The aforementioned characterizations were carried out at the raw bead locations. In this manner, we typically localized and tracked 7000-9000 beads within a 100 x 100 x 5 μm volume for each cell corresponding to an average bead to bead separation of ~1 μm. For experimental measurements of cell tractions, these displacements were next interpolated into a uniform grid with a mean nodal separation of 1.7 μm using Delaunay triangulation

and standard tri-linear shape functions in Matlab. By interpolating the displacements of randomly distributed beads onto a uniform grid (that was consistent between all measurements), we only have to compute a single discretized Green's function and singular value decomposition (as described below) and thus dramatically reduce the computational time for each traction measurement (e.g. from ~24 hours per traction measurement to ~10 minutes). The effect of this displacement interpolation was explicitly accounted for in all characterizations of resolution and sensitivity described below.

Hydrogel synthesis, mechanical characterization and measurement of Poisson ratio

Dry PEG (MW 6000; Sigma-Aldrich, St. Louis, MO) was reacted with acryloyl chloride and triethylamine (TEA) in anhydrous dichloromethane under argon to yield PEG-diacrylate (PEGDA). Separately, PEG-RGDS macromers were generated by reacting PEGDA with monocysteins CGRGDS peptides by dissolution in 100mM sodium phosphate, pH 8.0, followed by filtration through a 0.22 μm PVDF membrane (Millipore, Billerica, MA), dialysis, and lyophilization. To make flexible substrates for TFM experiments, PEGDA and acryloyl PEG-RGDS macromers were dissolved in phosphate buffered saline (PBS) pH 7.4, to final concentrations of 5.5 wt. % and 10 mM, respectively. These pre-polymer solutions were mixed with 0.2 μm diameter, non-functionalized fluorescent beads (suncoast yellow; Bangs Labs, Fishers, IN). The mixture was dispensed onto coverslips that were functionalized with 3-(trimethoxysilyl)propyl methacrylate (Sigma-Aldrich) and flattened by top coverslips, treated with SurfaSil (Thermo Scientific, Waltham, MA) per the manufacturer's instructions. The pre-polymer mixture between the coverslips was polymerized with 100 mW/cm^2 long-wavelength UV light (320-500 nm) for 30 sec using Omnicure S2000 (Lumen Dynamics, Mississauga, Canada). After removal of the top coverslip, the substrates were incubated in PBS at 37 °C for at least 24 hours to allow swelling.

A shear modulus of 2431 ± 87 Pa for the PEG hydrogels was measured using an AR 2000 rheometer (TA Instruments, New Castle, DE), equipped with a temperature-controlled Peltier plate at 37 °C and a 20 mm stainless steel plate geometry. Hydrogel samples were prepared and swollen using identical reagents and methods

26

as the substrates for the 2.5D TFM experiments. With the geometry head in contact with the hydrogel, strain sweeps of 1 % and 5 % at 0.25 Hz were performed, followed by frequency sweeps from 0.1 – 10 Hz at 1 % strain. Data were collected from multiple measurements of three independent samples.

A Poisson ratio of 0.34 was measured using cylinders laden with fluorescent beads. Each cylinder was cast within PDMS molds, polymerized and allowed to swell overnight. After swelling, the ends of the cylinder were glued to silanized glass slides using additional PEG prepolymer. The glass slides were then attached to a micrometer which was mounted above the microscope objective. The entire hydrogel was immersed in PBS for the duration of the experiment (**Figure S3A, B**). From a resting length of 10 mm, the cylinder was stretched to 5% (10.5 mm) and 10% (11 mm) strain. After each stretch, the hydrogel was allowed to re-equilibrate for 30 minutes to allow for any viscoelastic relaxation. Z-stacks were acquired for the entire thickness of the hydrogel at each strain (stretched along the y axis); however, because system was mounted on a widefield microscope (as opposed to a confocal), three-dimensional tracking was not able to be performed. Instead, a maximum intensity projection was taken from the central 0.1 mm of the cylinder and the 2D bead displacements were tracked (**Figure S3C**). Bead displacements were computed at both 5 and 10% strain. X and y displacement were plotted as a function of x and y position (as measured from the centerline of the cylinder) respectively and linear fits to each dataset, along with fitting parameters were computed (**Figure S3D**). The Poisson of 0.34 at both 5 and 10% strains (**Figure S3E**) was computed according to

$$n = -\frac{dx}{x}\frac{y}{dy} \qquad \textbf{(20)}$$

The Young's modulus of 6517 Pa was calculated from the shear modulus using the PEG Poisson ratio of 0.34 and assuming linearly elastic, isotropic material properties. In contrast to inferring the Poisson ratio based on confined and unconfined measurements of the Young's and bulk moduli, this direct approach allows for the possibility that water can be absorbed or exuded from the deformed polymer network and thus more accurately mirrors the experimental conditions.

Generation of a discretized Green's function

From linear elasticity, the displacement field $\overline{u}(\overline{r})$ within a continuum is related to the traction field $\overline{T}(\overline{r}')$ at a point via a Green's function $\Gamma(\overline{r}, \overline{r}')$ and a Fredholm integral of the first kind:

$$\overline{u}(\overline{r}) = \int \Gamma(\overline{r}, \overline{r}') \, \overline{T}(\overline{r}') \, \mathrm{d}\overline{r} \qquad \textbf{(21)}$$

Solving for the traction field $\overline{T}(\overline{r}')$ requires knowledge of a suitable Green's function $\Gamma(\overline{r}, \overline{r}')$ and inversion (or differentiation) of equation 21 The inversion of a noise-contaminated displacement field $\overline{u}(\overline{r})$ renders the problem very sensitive to high frequency fluctuations in $\overline{u}(\overline{r})$ which are often attributed to errors in measurement. For this reason, the problem is ill-posed and requires some form of regularization (or smoothing of the displacement measurements) in order to obtain a reasonable solution.

To implement this approach, we generated a discretized Green's function relating tractions on the hydrogel surface to displacements within the gel using the finite element method. To approximate a semi-infinite halfspace, we generated a 3D tetrahedral mesh of a 300 μm wide by 300 μm long by 60 μm tall volume using Abaqus CAE. A 100 μm square central portion of the top surface corresponding to the field of view for our microscopic images was discretized separately to have 11204 triangular elements, corresponding to an average element area of approximately 0.9 μm^2. We then solved the forward finite element solution under the linear small strain approximation to relate the nodal displacements in the gel to unit tractions applied to each facet on the aforementioned surface in each of the three Cartesian directions (33612 total solutions). Because this method only requires a single decomposition of the FE stiffness matrix, it is considerably faster than numerical integration of the Greens function over each element as was done previously (6, 7). From each of these solutions, the displacement grid locations were queried for the computed displacements. Because both the bead coordinates and the location of applied tractions are at discrete locations, the relation between bead displacements within the gel $\overline{u}$ and tractions on the surface of the cell $\overline{T}$ is now transformed into a set of linear equations

$$\bar{u} = \Gamma \bar{T} \qquad (22)$$

where we have adopted the notation used in (8) in which

$$\bar{u} = [u_1(\bar{r}_1); u_2(\bar{r}_1); u_3(\bar{r}_1); u_1(\bar{r}_2); u_2(\bar{r}_2); u_3(\bar{r}_2); \dots; u_1(\bar{r}_m); u_2(\bar{r}_m); u_3(\bar{r}_m)] \qquad (23)$$

is a 3m column vector, where m is the number of tracked beads and $\bar{r}$ is the position vector of each bead.

$$\bar{T} = [T_1(\bar{r}_1'); T_2(\bar{r}_1'); T_3(\bar{r}_1'); T_1(\bar{r}_2'); T_2(\bar{r}_2'); T_3(\bar{r}_2'); \dots; T_1(\bar{r}_n'); T_2(\bar{r}_n'); T_3(\bar{r}_n')] \qquad (24)$$

is a 3n column vector, where n is the number of discretized facets on the surface of the cell and $\bar{r}'$ is the position vector of each facet. Subscripts for both u and T in these definitions represent displacements and tractions respectively along each Cartesian axis.

Γ is an m x n matrix of the following form:

$$\Gamma_{ij}^{mn} = \begin{bmatrix} G_{ij}^{11} & \cdots & G_{ij}^{1n} \\ \vdots & \ddots & \vdots \\ G_{ij}^{m1} & \cdots & G_{ij}^{mn} \end{bmatrix} \qquad (25)$$

Each element of Γ is a 3 x 3 submatrix relating the displacement of bead m in direction i in response to a load on facet n in direction j:

$$G_{ij} = \begin{bmatrix} g_{11} & g_{12} & g_{13} \\ g_{21} & g_{22} & g_{23} \\ g_{31} & g_{32} & g_{33} \end{bmatrix} \qquad (26)$$

Solution of the inverse problem utilizing the L-curve

As described previously (7-9), relating the displacement measurements within the hydrogel volume to traction measurements at the hydrogel surface is an ill-posed, inverse problem that requires regularization in order to obtain a reasonable solution. To this end, we used 0th order Tikhonov regularization together with the L-curve criterion (10) for implementing and choosing the correct value for the Lagrange parameter, λ resulting in the following optimization:

$$min\{|\mathbf{\Gamma}\overline{T} - \overline{u}|^2 + \lambda^2|\overline{T}|^2\} \qquad \textbf{(27)}$$

This approach relies on the fact that a log-log plot of $|\overline{T}|^2$ vs. $|\mathbf{\Gamma}\overline{T} - \overline{u}|^2$ as a function of λ^2 often resembles an "L" shape. The optimal tradeoff between matching the experimental bead displacements (i.e. minimizing $|\mathbf{\Gamma}\overline{T} - \overline{u}|^2$) and maintaining reasonable traction magnitudes (i.e. minimizing $|\overline{T}|^2$) occurs near the corner of this curve. Similar to previous implementations (5, 8, 11), this optimization problem was solved by singular value decomposition using the suite of Matlab routines "*Regularization tools*" by PC Hansen (12).

Note, the Green's function and tractions above are calculated to transition from the reference, stress-free configuration of the substrate to its deformed, stressed configuration. We therefore solve for the surface tractions that would need to be applied on the reference configuration in order to cause the cell-induced displacements. Results indicated that under the small strain approximation, changes in volumes/areas are minimal and the material stresses approximate the true Cauchy stresses. To better relate the locations of these tractions to the immunofluorescent images of the cells (which are obtained in the stressed configuration - prior to SDS treatment), we projected these computed tractions onto the stressed configuration (i.e. projected the material stresses/surface tractions onto the deformed geometry). The algorithm we chose for convenience was to generate a separate

discretized Green's function Γ' that relates the displacement of the surface nodes (rather than the bead locations in the bulk) to surface tractions. We then solved

$$\overline{\boldsymbol{u}}' = \Gamma'\overline{\boldsymbol{T}} \qquad \textbf{(28)}$$

where Γ' is the Green's function that relates surface tractions to surface node displacements, $\overline{\boldsymbol{T}}$ is the recovered traction vector (recovered from equation 27), and $\overline{\boldsymbol{u}}'$ are the displacements of the surface nodes in order to deform the relaxed (reference) geometry into the stressed (deformed) geometry. Note that because the stress-strain equations are linear under the small strain assumption, this is fundamentally equivalent to solving the finite element equations for the surface displacements in response to the tractions $\overline{\boldsymbol{T}}$ that match the bead displacements in the bulk.

Use of the L-curve is well established in solving inverse problems and for traction force microscopy (5, 8, 11); nevertheless, we also investigated the behavior of the solution in the vicinity of the corner of the L-curve to determine how sensitive the reported tractions are to the parameter λ^2 (**Figure S14**). For all cells measured, the L-curved displayed a well-defined maximum in curvature (i.e. a clear corner). When λ^2 is *decreased* below the value indicated by this corner, the tractions begin to increase exponentially in magnitude and background noise increases dramatically. When λ^2 is *increased* above the corner value, the tractions decrease in magnitude slowly, but the errors in matching the bead displacements increase significantly. However, while the absolute magnitudes of the tractions vary significantly, the spatial relationship of the tractions are qualitatively similar even when λ^2 varies over a full order of magnitude. Importantly, rotational moments about peripheral adhesive regions were maintained over this range (**Figure S14**).

For display purposes, all renderings of cellular tractions were computed in Tecplot 360 (Tecplot Inc., Bellevue, WA), and contour plots were scaled such that approximately 1 % of all elements on the cell were saturated.

Characterization of resolution and sensitivity

A quantitative characterization of resolution of the reported tractions is complicated by the vectorial relationship between tractions and displacements. Qualitatively, a traction applied uniformly over a large area would introduce displacements of many beads and should therefore be easier to detect than a punctuate traction which will only introduce displacements of a small subset of beads that are nearby. That is, because traction is reported as a force per unit area, the total energy (or force) imparted by a widely distributed surface traction would be significantly higher than that imparted by a surface traction of identical magnitude which is confined to a small area. Thus reporting that a traction reconstruction has a *sensitivity* of ** Pa without any mention to the area across which such tractions were measured is meaningless. Similarly, reporting that a traction reconstruction has a *resolution* of ** μm without any mention as to the magnitude of the tractions capable of being measured at this length scale is also meaningless. Thus, in traction force microscopies, resolution and sensitivity are inherently linked.

Further complicating the analysis of resolution, two traction vectors in close proximity will produce displacements within the hydrogel that could either add constructively or act to cancel each other out depending on whether the traction vectors are aligned or opposed. Thus, the directions at which surface tractions are oriented will also impact the true resolution and sensitivity of the technique. In order to address each of these aspects (spatial resolution, traction sensitivity, and the effect of traction orientation of these two factors), we utilized simulated datasets and two different metrics to characterize our technique. In the first approach, we computationally generated uniform tractions aligned with the x, y, or z Cartesian directions that were distributed over a circle of defined radius. The forward FEM solution was computed and the displacements calculated at specific locations within the hydrogel with densities and distributions that mirrored experimental bead densities and distributions. Gaussian distributed noise, scaled by the experimentally measured errors (**Figure S2B**) was then added to these displacement measurements. These noisy measurements were then interpolated onto the same grid as was used for experimental measurements and the tractions recovered in an identical manner (i.e. under L-curve regularization). The magnitude of the simulated tractions and the radius of the circle over which they were distributed were progressively decreased until we could no longer recover the simulated tractions (**Figure S4**). In

order to be as general as possible, the loadings were scaled according to % of the hydrogel elastic modulus and can thus be applied to all the hydrogels used in this study. For reference, a table of % elastic modulus to traction Pa is provided in **Table S1** for each of the hydrogels used in this study. In this work, we only consider errors introduced by the finite sampling of the displacement field and the displacement measurement noise. For small displacements, the stress-strain equations are linear, and the errors introduced by the FEM discretization of the Green's function should be negligible in comparison to the previous two factors. However, for large displacements, or coarsely discretized finite element meshes, this may become a significant factor (as was previously characterized in (5)).

As the radius of the circle upon which the tractions were applied decreased, the recovered tractions progressively began to underestimate the magnitude of the true loading and over estimate the spatial area over which the loading was applied, effectively blurring or averaging the true loading (**Figure S5-S7**). This effect was present for both shear and normally applied loadings and became more pronounced as the magnitude of the applied tractions decreased. In each of the three Cartesian directions, there exists a point at which it becomes difficult for our technique to discern between different conditions (gray boxes in **Figures S5-S7**). For both shear and normal loadings, our method would thus report a 5% load distributed over a ~10 μm radius circle even if the true traction distribution were a 10% load applied over a 5 μm radius circle, a 25% load applied over a 3 μm radius circle, or a 50% load applied over a 2 μm radius circle. This resolution vs. sensitivity line roughly represents the limits of our technique for isolated, punctuate loadings with a full-width half-maximum of ~10 μm (**Figure S8**). Everything above this line can be resolved accurately; everything below this line will be underestimated and blurred to within this threshold. It is apparent from looking at the plots of **figures S5-S7** that this metric is conservative, for normal loads, we can in fact detect a 10% load applied over a 3 μm radius circle and a 5% load applied over a 5 μm radius circle.

The above discussion is useful for characterizing the spatial resolution of traction measurements; however, it is important to keep in mind that this metric only represents the resolution for isolated, punctuate loads. Such loadings are often more difficult to recover because the limited spatial extent of the applied loadings means that only a small fraction of the beads will have detectable displacements and thus detectible signal to noise. Because there is no way of knowing a-priori where the force is localized, all beads must be incorporated into the solution even though many of them will only serve to contaminate the system with error. Previous implementations have attempted to circumvent this by restricting recovered tractions to occur only at focal adhesions (13). While this may be reasonable for 2D measurements of only shear loadings, it does not apply for our 2.5D method where the cortex of the cell may be expected to exert pressure on the substrate in regions where adhesions are not detected.

In order to address the effect of traction orientation on resolution we adopted a different set of simulated loadings. Oscillatory loadings were applied across a region of the substrate that encompassed the entire experimental field of view (**Figure S9**). These loadings were oriented as either parallel shear tractions, perpendicular shear tractions, or normal tractions (**Figure S10A**). The recovered tractions were computed in an identical manner to that described above and compared to the original loadings. Under each condition, the wavelength and the magnitude of the simulated loadings were progressively decreased until the tractions could no longer be recovered. The errors in the recovered tractions were compared quantitatively according to

$$\% \ traction \ error = \frac{|Ts - Tr|_2}{|Ts|_2} \times 100 \quad \textbf{(29)}$$

where Ts and Tr are the simulated loadings and recovered loadings respectively and the norms are the Euclidian norm (**Figure S10B**). Note that such a global analysis is not appropriate for the spatially isolated traction analysis above because the vast majority of the simulated traction components in those cases are zero, thus any background would add disproportionately to the global error. We found that oscillatory shear loadings directed parallel to each other were the most difficult to recover. In all conditions, the accuracy of traction recovery

34

decreased with both the wavelength and magnitude of the applied loadings. A graphical depiction of the errors as presented in **Figure S10B** is shown in **Figure S10C**. An error of 25% indicates that the recovered traction vector will lie within a sphere centered at the tip of the simulated traction vector with a radius that is 25% of the magnitude of Ts. This is the 3D vectorial equivalent to traditional error bars on a 1D plot. While the error described above provides a quantitative metric for the accuracy of the recovered tractions, it can be difficult to interpret qualitatively. Because the simulated tractions are applied only along a specific Cartesian direction whereas the errors in the recovered tractions will be distributed across all Cartesian directions, this metric appears to be overly pessimistic (e.g. significant information about the simulated loadings can be obtained even at the 100% global error point). To illustrate this, we have plotted line cuts of the simulated and recovered tractions for both 5% (**Figure S11**) and 2% (**Figure S12**) simulated traction magnitudes. For example for normal loadings of 2% the hydrogel elastic modulus, oscillating at 10 μm wavelength (**Figure S12**) one can still readily discern the oscillatory nature of the simulated loading, albeit at the cost of significant background in both the x and y components.

The simulations presented here are well-controlled metrics for assessing the resolution and sensitivity limits of traction force microscopy techniques. In contrast, cells exert neither continuously oscillating loads, nor spatially isolated punctuate loads. Nevertheless, the metrics presented here serve to characterize the two extremes of recoverable loadings and thus quantitatively assess the resolution and sensitivity of the system. Moreover, these metrics could be readily applied to compare the benefits of previous and new developments to traction force microscopy methods or to quantitatively test the potential advantages of various approaches.

Bootstrap analysis of reported tractions and global force balance

The experimentally recovered tractions will represent a spatially averaged or blurred "image" of the true traction loadings subject to limitations presented in the preceding section. Given this constraint, it is also important to determine the statistical significance of the reported tractions. Put another way, one can ask – if we were to measure the displacement field a number of different times, and given that each measurement will be subject to

some randomly distributed experimental noise, how much variation could we expect in the recovered tractions? Because the cell (and thus the tractions) are not temporally constant, acquiring multiple experimental measurements of the same traction field is not feasible. However, one can assess the significance of the recovered tractions a-posteriori via a bootstrap analysis (5, 7, 8). In this method, the recovered tractions are used to generate displacements at the measured bead locations via solution of **equation 22**. Experimentally relevant levels of noise are then superimposed onto these displacements before interpolating onto the same grid used in the initial traction measurement. **Equation 27** is then solved using the L-curve criterion and the newly recovered tractions compared to the initial measurement. This process can then be repeated numerous times to assess the statistical significance of the reported tractions. To verify that the reported tractions and specifically that the presence of rotational moments about peripheral adhesions were statistically robust, we performed 100 bootstrap iterations for traction measurements of 3 separate cells (**Figure S13**). The compiled standard deviations in the recovered tractions were ~7Pa in x and y and ~20 Pa in Z (**Figure S13A**). For each of the cells tested, we show the mean recovered bootstrap tractions, culled to show only those tractions with components that were each greater than 2 standard deviations of the bootstrap measurements (**Figure S13B**). Although the bootstrap analysis resulted in a further smoothing of the traction fields (as evidenced by the lower magnitude tractions as compared to **Figure 2**), both the centrally localized shear maxima and the rotational moment about actin fibers and adhesions were statistically significant.

We also note that when the entire cell is within the microscope field of view, one might expect the forces exerted by the cell to satisfy a global force balance. This balance is not implicitly enforced in our algorithm, and thus deviation from this balance provides some insight into the magnitude of the errors in the reported tractions. The relative errors in this balance expressed as

$$\% \, force \, error = \frac{abs(\sum_{i=1}^{n} F_i)}{(\sum_{i=1}^{n} abs(F_i))} \times 100 \qquad (30)$$

summed over all n forces, where F is the traction component on either the x, y or z direction divided by the element area across which the traction is distributed, were typically between 1 and 5% for both the lateral and axial Cartesian directions.

Effect of substrate stiffness

We also investigated whether rotational moments about adhesions were only limited to cells cultured on relatively rigid hydrogels. By varying the weight percent of the PEGDA while keeping the concentration of PEG-RGDS constant, we could tune the material stiffness independent of changes in adhesive ligand. We generated 3 hydrogels with elastic moduli of 1160 Pa (soft), 4756 Pa (medium), and 6517 Pa (stiff) and cultured MEF cells on each substrate. As the stiffness of the substrate increased, cells spread to a greater extent and exerted progressively stronger shear and normal tractions (**Figure S16A-C**). Although previous studies have reported strong downward tractions under the nucleus of cells, in our system and at each substrate stiffness, both the shear and normal tractions were largely limited to the cell periphery. We did observe weak downward tractions under the nucleus of cells in the very early stages of cell spreading. Thus while nuclear compression may explain the downward forces observed in some settings, this does not appear to apply to all cell types or across all hydrogel conditions (14). Finally, we observed that the ratio of total normal traction to total shear traction exerted by cells decreased progressively as the substrate became stiffer (**Figure S16D**), suggesting that the relative importance of normal tractions may be enhanced when cells are cultured on soft vs. rigid substrates.

Segmentation and averaging of peripheral adhesive regions

In order to reveal trends across multiple adhesions and multiple cells, we developed an algorithm to average the displacements and tractions in the vicinity of peripheral adhesions. Peripheral adhesions were outlined by hand from maximum intensity projections of EGFP-paxillin expressing MEFs. Only elongated adhesions were selected. If multiple adhesions were distributed serially (i.e. radially one behind the other) then they were grouped into a single "adhesive region". These images were then used to generate a binary mask and imported into Matlab. Ellipses were fit to each isolated region using the "BWLABEL and REGIONPROPS" functions (**Figure S19**,

green outlines) and major and minor axis determined. For all adhesions measured (121 adhesions from 10 cells), the mean major and minor axis were 8.3 ± 3.9 µm and 2.17 ± 0.9 µm respectively. Co-centric, expanded ellipses of 2X the major and minor axis were then generated around each adhesion (**Figure S19**, magenta outlines) and tractions and displacements compiled within this expanded region. Displacements and tractions within these regions were then plotted according to their projected distance along the major axis of fitted ellipse. In order to compare adhesions of different lengths and widths, the projected distance was normalized by dividing by the length of the major axis fit of each adhesion. Traction measurements were further normalized by dividing both the shear and normal tractions by the maximum amplitude of the shear traction in the isolated region.

Finite element details and discussion

To model how cytoskeletal forces applied to focal adhesions could lead to rotational moments, we generated a finite element model of one focal adhesion in contact with the adhesive PEG hydrogel. The PEG hydrogel was modeled in Abaqus as a 200 x 200 x 60 µm cube with *ENCASTRE boundary conditions along the bottom surface. The material was treated as a NeoHookean solid according to

$$U = C_{10}(\bar{I}_1 - 3) + \frac{1}{D_1}(J^{el} - 1)^2 \qquad \textbf{(31)}$$

where U is the strain energy per unit of reference volume, C_{10} and D_1 are material parameters, $\bar{I}_1 = \bar{\lambda}_1^2 + \bar{\lambda}_2^2 + \bar{\lambda}_3^2$ is the first deviatoric strain invariant. The deviatoric stretches are defined as $\bar{\lambda}_i = J^{-\frac{1}{3}}\lambda_i$ where λ_i are the principal stretches and J is the total volume ratio. $J^{el} = J$ for isothermal conditions. The initial shear modulus and bulk modulus are given by $\mu_0 = 2C_{10}$ and $\kappa_0 = \frac{2}{D_1}$ respectively. Values of C_{10} and D_1 were computed using the measured shear modulus of 2431 Pa. The bulk modulus was computed based on a measured Poisson ratio for the PEG hydrogels of 0.34 via $\kappa_0 = \frac{2\mu_0(1+v)}{3(1-2v)}$ as 6787 Pa. All simulations were modeled

38

utilizing a symmetry boundary condition cutting vertically through the major axis of the adhesion (bisecting it). The focal adhesion was modeled as a 150 nm tall elliptical plate with major and minor axis of 6 and 2 μm respectively (**Figure S15**). The focal adhesion material was treated as linearly elastic with a Young's modulus of 2.4MPa and a Poisson ratio of 0.49 (effectively a rigid, incompressible plate). The bottom surface of the adhesion was anchored to the PEG hydrogel using the surface to surface *TIE constraint in Abaqus. A surface traction was applied to the upper surface of the adhesion using *DSLOAD in Abaqus. Because the actin cable applying this traction in cells is expected to remain taught, the applied load was kept parallel to x-y plane of the substrate (i.e. it did not rotate with the surface of the adhesion). The magnitude of this traction was increased until the horizontal displacements of the hydrogel matched those observed experimentally. An optimal match for the horizontal displacements was observed for an applied traction of approximately 3.128kPa when distributed uniformly on the dorsal surface of the adhesion.

This model of a uniform shear load applied to a rigid focal adhesion that is uniformly coupled to the substrate is, to our knowledge, the simplest model capable of reproducing the displacement patterns we observe experimentally. In order to generate a significant moment, the adhesion must be significantly stiffer than the underlying substrate. Our approximation of the adhesion as an essentially rigid plate is certainly an overestimate of the stiffness; however, this requirement may be relaxed if other factors such as the surrounding ventral cortex, or additional attachment to the dorsal actin meshwork, were to be included. Moreover, nearly all measurements of the mechanical properties of cells have been obtained from measuring the dorsal surface, which may be significantly weaker than the ventral surface. Indeed, the fact that we observe slowly decaying downward displacements proximal to the adhesion (which cannot be accurately captured by our simple model) suggests that the ventral cortex may also be generating significant downward tractions on the surface. Indeed recent super-resolution studies (15) have revealed what appears to be a buckling of the ventral actin cortex, which would support this hypothesis.

Supplementary References

1. Raeber GP, Lutolf MP, & Hubbell JA (2005) Molecularly engineered PEG hydrogels: a novel model system for proteolytically mediated cell migration. *Biophysical journal* 89(2):1374-1388.
2. Crocker JC & Grier DG (1996) Methods of digital video microscopy for colloidal studies. *J Colloid Interf Sci* 179(1):298-310.
3. Gao YX & Kilfoil ML (2009) Accurate detection and complete tracking of large populations of features in three dimensions. *Opt Express* 17(6):4685-4704.
4. Smith CS, Joseph N, Rieger B, & Lidke KA (2010) Fast, single-molecule localization that achieves theoretically minimum uncertainty. *Nature methods* 7(5):373-375.
5. Legant WR*, et al.* (2010) Measurement of mechanical tractions exerted by cells in three-dimensional matrices. *Nature methods* 7(12):969-971.
6. Delanoe-Ayari H, Rieu JP, & Sano M (2010) 4D traction force microscopy reveals asymmetric cortical forces in migrating Dictyostelium cells. *Physical review letters* 105(24):248103.
7. Dembo M, Oliver T, Ishihara A, & Jacobson K (1996) Imaging the traction stresses exerted by locomoting cells with the elastic substratum method. *Biophysical journal* 70(4):2008-2022.
8. Schwarz US*, et al.* (2002) Calculation of forces at focal adhesions from elastic substrate data: the effect of localized force and the need for regularization. *Biophysical journal* 83(3):1380-1394.
9. Ambrosi D (2006) Cellular traction as an inverse problem. *Siam J Appl Math* 66(6):2049-2060.
10. Hansen PC (2001) The L-Curve and its use in the numerical treatment of inverse problems. *Computational Inverse Problems in electrocardiography (Advances in Computational Bioengineering)*, ed Johnston PR (WIT Press, Southampton), Vol 5, pp 119-142.
11. Sabass B, Gardel ML, Waterman CM, & Schwarz US (2008) High resolution traction force microscopy based on experimental and computational advances. *Biophysical journal* 94(1):207-220.
12. Hansen PC (2007) Regularization Tools Version 4.0 for Matlab 7.3. *Numerical Algorithms* 46(2):189-194.
13. Balaban NQ*, et al.* (2001) Force and focal adhesion assembly: a close relationship studied using elastic micropatterned substrates. *Nature cell biology* 3(5):466-472.
14. Hersen P & Ladoux B (2011) Biophysics: Push it, pull it. *Nature* 470(7334):340-341.
15. Xu K, Babcock HP, & Zhuang X (2012) Dual-objective STORM reveals three-dimensional filament organization in the actin cytoskeleton. *Nature methods* 9(2):185-188.
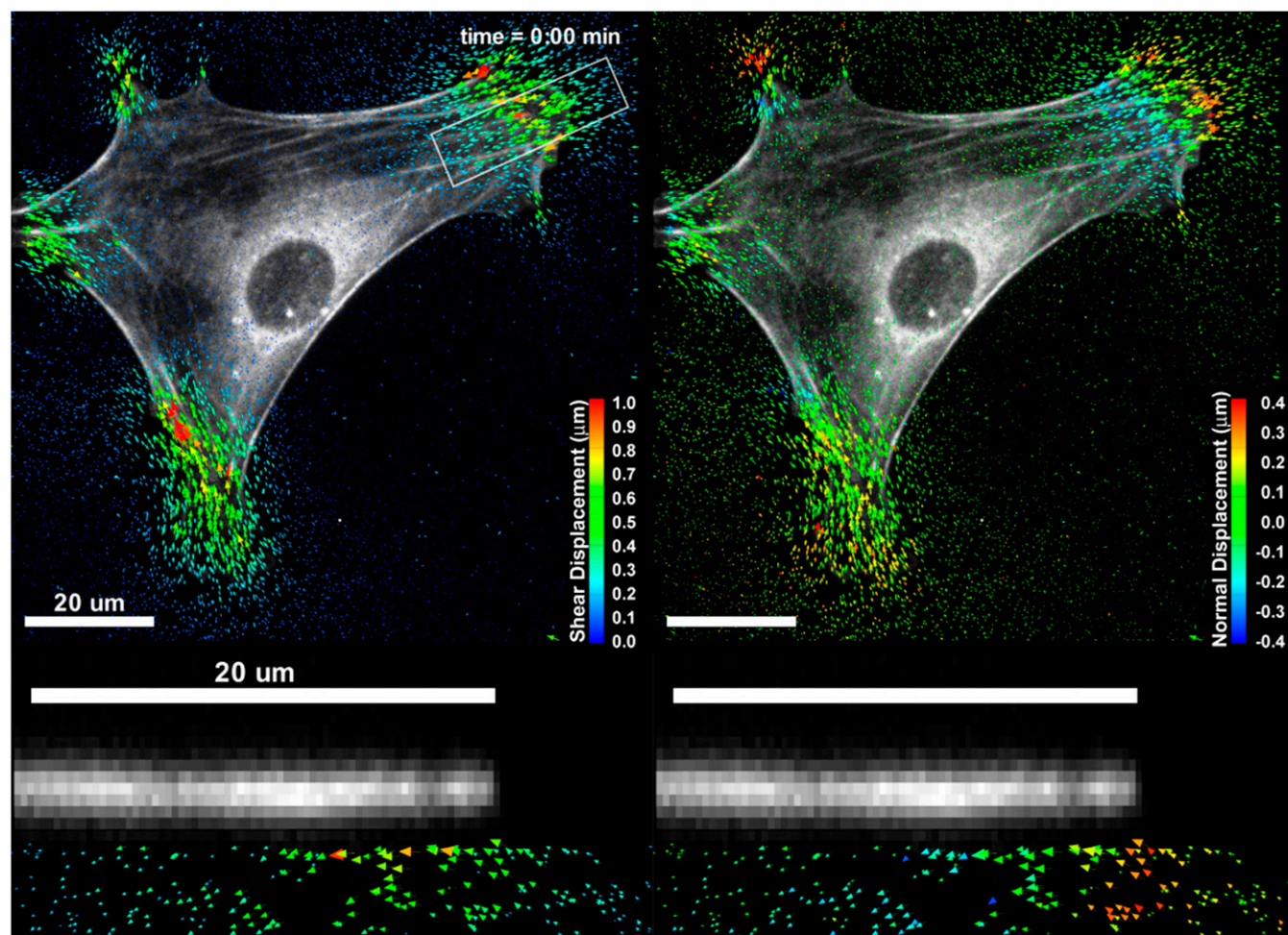
# Supporting Information

Legant et al. 10.1073/pnas.1207997110
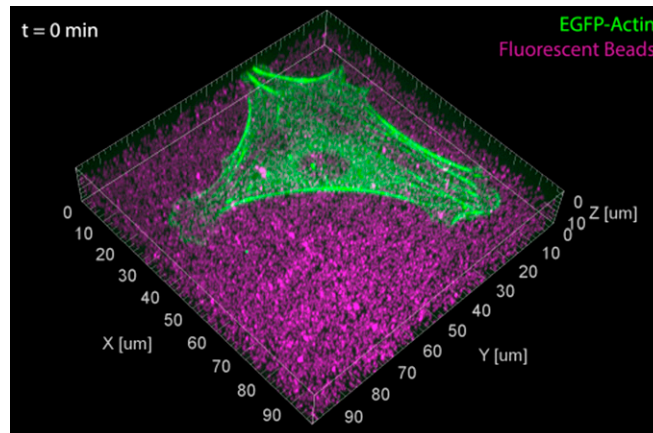
Movie S1. Volume rendering of an EGFP-actin–expressing MEF cultured on top of a planar PEG hydrogel containing fluorescent beads.
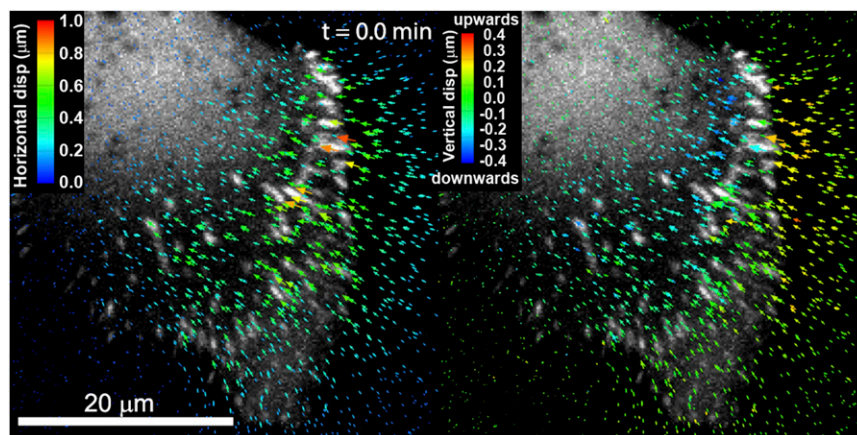
Movie S1

Movie S2. Hydrogel displacements induced by the EGFP-actin–expressing cell shown in Movie S1. Displacements are computed from tracking fluorescent beads before and after treatment with SDS. Horizontal (shear) displacements are shown on *Left* and vertical (normal) displacements are shown at *Right*. For vertical displacements, red indicates an upward displacement toward the dorsal surface of the cell and blue indicates a downward displacement into the hydrogel. Cross-section views in the bottom frames are taken from the white outlined region indicated at *Top*. (Scale bars, 20 μm.)
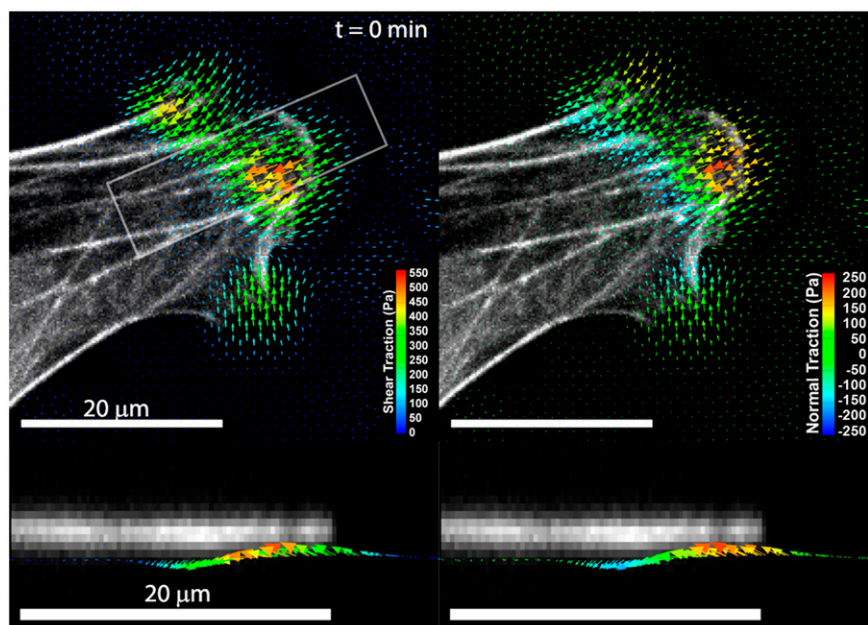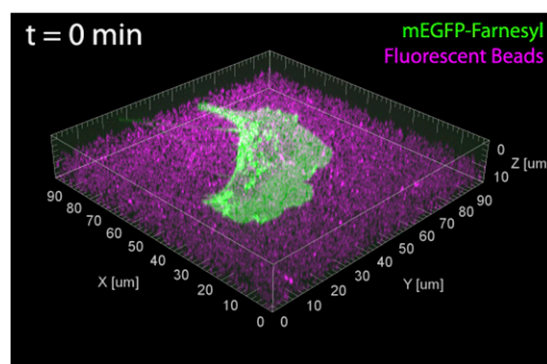
Movie S2

Movie S3. Cell tractions exerted by the EGFP-actin–expressing cell shown in Movie S1. Shear tractions are shown on *Left* and normal tractions are shown at *Right*. For vertical tractions, red indicates an upward pulling force toward the dorsal surface of the cell and blue indicates a downward pushing force into the hydrogel. Cross-section views in the bottom frames are taken from the white outlined region indicated at *Top*. (Scale bars, 20 μm.)

Movie S3

Movie S4. Bead displacements induced by the paxillin-EGFP–expressing cell shown in Fig. 2 *E–H*. Horizontal displacements are shown on the *Left* and vertical displacements are shown at *Right*. For vertical displacements, red indicates an upward displacement toward the dorsal surface of the cell and blue indicates a downward displacement into the hydrogel. (Scale bars, 20 μm.)
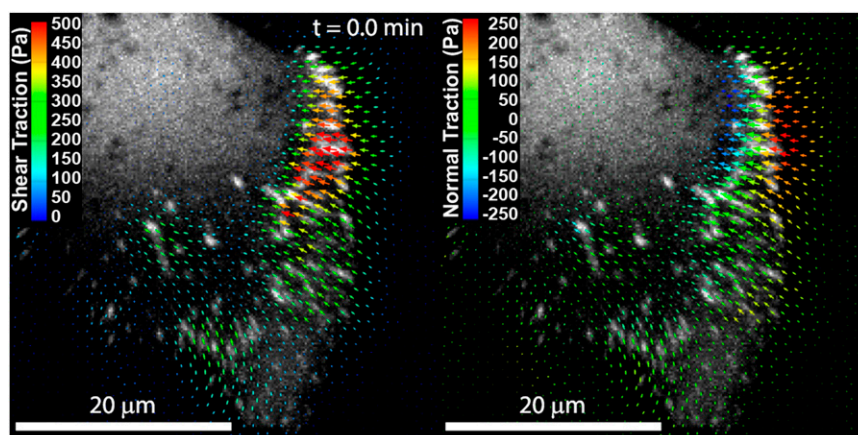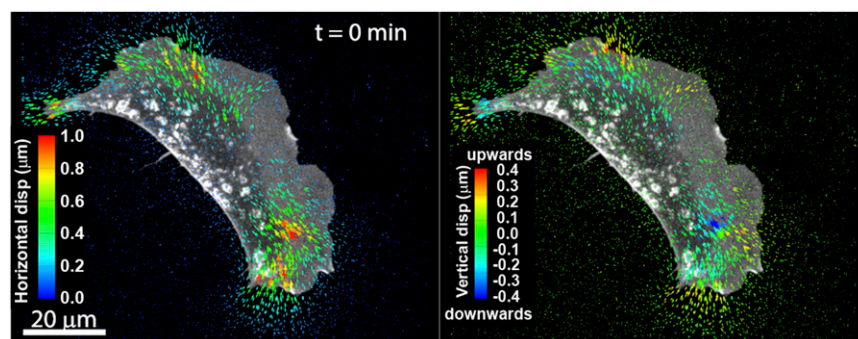
Movie S4

Movie S5. Cell tractions exerted by the paxillin-EGFP–expressing cell shown in Fig. 2 *E–H*. Shear tractions are shown on the *Left* and normal tractions are shown at *Right*. For normal tractions, red indicates an upward pulling force toward the dorsal surface of the cell and blue indicates a downward pushing force into the hydrogel. (Scale bars, 20 μm.)
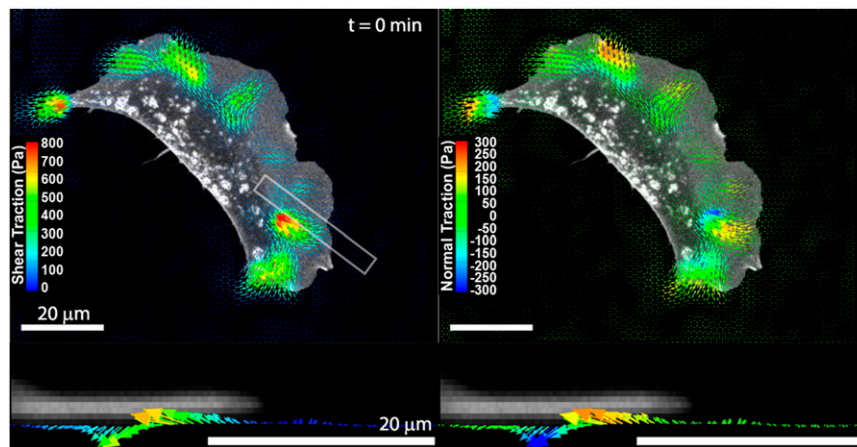
Movie S5

Movie S6. Volume rendering of an mEGFP-farnesyl–expressing MEF migrating on top of a planar PEG hydrogel containing fluorescent beads.
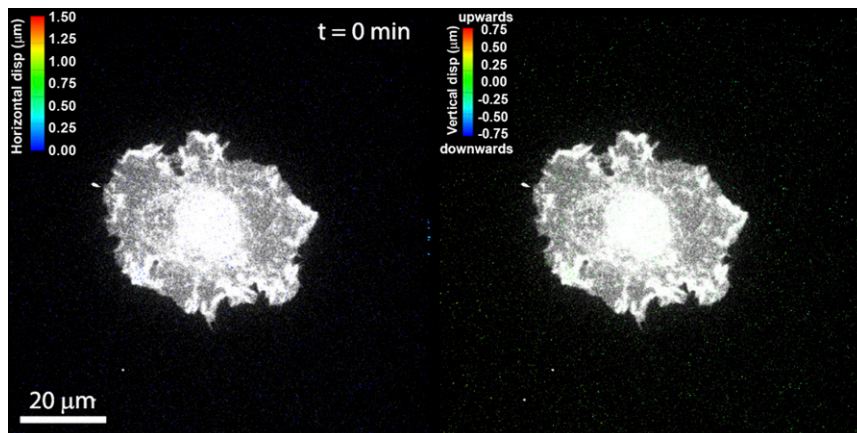
Movie S6

Movie S7. Bead displacements induced by the mEGFP-farnesyl–expressing cell shown in Movie S6. Horizontal displacements are shown on the *Left* and vertical displacements are shown at *Right*. For vertical displacements, red indicates an upward displacement toward the dorsal surface of the cell and blue indicates a downward displacement into the hydrogel. (Scale bars, 20 μm.)
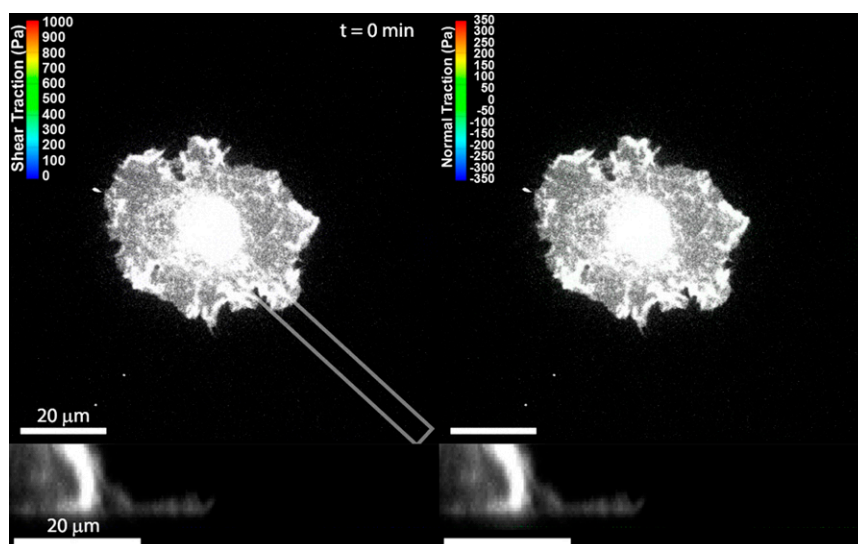
Movie S7

Movie S8. Cell tractions exerted by the mEGFP-farnesyl–expressing cell shown in Movie S5. Shear tractions are shown on the *Left* and normal tractions are shown at *Right*. For vertical tractions, red indicates an upward pulling force toward the dorsal surface of the cell and blue indicates a downward pushing force into the hydrogel. Cross-section views in the *Lower* frames are taken from the white outlined region indicated at *Top*. (Scale bars, 20 μm.)

Movie S8

Movie S9. Bead displacements induced during the initial spreading of an mEGFP-farnesyl–expressing cell on top of a planar PEG hydrogel. Horizontal displacements are shown on the *Left* and vertical displacements are shown at *Right*. For vertical displacements, red indicates an upward displacement toward the dorsal surface of the cell and blue indicates a downward displacement into the hydrogel. (Scale bars, 20 μm.)

Movie S9

Movie S10. Cell tractions exerted during the initial spreading of an mEGFP-farnesyl–expressing cell on top of a planar PEG hydrogel. Shear tractions are shown on *Left* and normal tractions are shown at *Right*. For vertical tractions, red indicates an upward pulling force toward the dorsal surface of the cell and blue indicates a downward pushing force into the hydrogel. Cross-section views in the *Lower* frames are taken from the white outlined region indicated at *Top*. (Scale bars, 20 μm.)

Movie S10

Other Supporting Information Files

SI Appendix (PDF)